

Influences of Ti and Mo alloying on the microstructure and properties of laser cladding for CoCrFeNi high-entropy alloys

Guofu Lian ^{a,b,1,*}, Jianghuai Yang ^{a,b,1}, Changrong Chen ^{a,b}, Xu Huang ^{a,b}, Meiyuan Feng ^{a,b}

^a School of Mechanical and Automotive Engineering, Fujian University of Technology, Fuzhou 350118, China

^b Fujian Key Laboratory of Intelligent Machining Technology and Equipment, Fujian University of Technology, Fujian Fuzhou 350118, China

ARTICLE INFO

Keywords:

Laser cladding
High-entropy alloys
The first-principles calculation
Bi-phase synergy
Property

ABSTRACT

The CoCrFeNiTi_{1-(x)}Mo_x high-entropy-alloy coating was prepared using a powder presetting method. The work investigated the influences of Ti and Mo addition on the microstructure and properties of CoCrFeNi high-entropy alloys. The first-principles calculation showed that CoCrFeNiTi_{1-(x)}Mo_x was mainly composed of the FCC phase, BCC phase, and IMCs. The coating exhibited high hardness, and the mechanical stability of the high-entropy alloys of FCC and BCC phases was maintained when $x = 0.5$. The coating primarily consisted of FCC, BCC, and CoTi₂ phases when $x \leq 0.75$. The coating primarily consisted of FCC, BCC, and Co₂Mo₃ phases when $x = 1$. It exhibited high microhardness, elastic modulus, elastic stiffness, and wear resistance when $x = 0.5$. Its average microhardness, local elastic modulus, and elastic stiffness were 873.28 HV_{0.5}, 265.5606 GPa, and 102.8008 GPa, respectively. Besides, COF and the wear mass loss were 0.7026 mm³ and 0.0410 mm³, respectively. The coating exhibited exceptional corrosion resistance with a self-corrosion voltage of -0.700 V and a self-corrosion current of 5.387e-007 A when $x = 1$. The results offer practical guidance for preparing high-entropy-alloy coatings with various advantages as well as a theoretical foundation for preparing such alloys by laser cladding.

1. Introduction

The laser-cladding material is decisive for the microstructure and properties of the prepared coating [1,2]. Commonly employed cladding materials encompass autolytic alloy powders, ceramic hard-phase powders, composite powders, and novel high-entropy-alloy powders [3]. The main feature of high-entropy alloys lies in their inclusion of various pivotal elements, which enables the full utilization of the alloy's substrate effects. The alloys possess exceptional hardness, excellent corrosion resistance, and superior mechanical strength at elevated temperatures [4,5]. Therefore, it is a new research hotspot in metal materials.

Different types and content of high-entropy-alloy coating components affect the microstructure and properties of the coating. CoCrFeNi-based high-entropy alloys have attracted much attention for their excellent stretch performance at room temperature and low temperature. The addition of 1–2 elements to CoCrFeNi-based high-entropy alloys is a prominent research focus [6] for enhancing the overall performance of alloys. Ti addition enhances the alloy's hardness and

wear resistance [7] while Mo improves those properties in the coating [8].

Wang et al. [9] used the laser cladding to prepare the CoCrFeNiTi_x ($x = 0.1, 0.3, 0.5$, and 0.7) coating on Q235 steel. They studied the effect of changes in Ti content on the microstructure and properties of the coating. Ti addition significantly improves the coating properties with increased Ti content. Corrosion resistance is optimal and the hardness reaches its maximum when $x = 0.7$. Fu et al. [10] used the laser cladding to prepare CoCr₂FeNiMo_x ($x = 0, 0.1, 0.2, 0.3$, and 0.4) coating on Q235 steel. They studied the effects of changes in Mo content on the microstructure and properties of the coating. Mo addition significantly improves hardness and wear resistance. The CoCr₂FeNiMo_{0.3} coating exhibits excellent performance under the synergy of corrosion and wear in the 3.5 wt%NaCl solution.

Current research focuses on the influence of changes in a single element on the microstructure properties of the coating. There are few studies on simultaneous synergistic reinforcement through the addition of multiple elements. The influence of Ti and Mo alloying on CoCrFeNi-based high-entropy alloys was studied in the work. CoCrFeNiTi_{1-(x)}

* Corresponding author. School of Mechanical and Automotive Engineering, Fujian University of Technology, Fuzhou 350118, China.

E-mail address: gflian@mail.ustc.edu.cn (G. Lian).

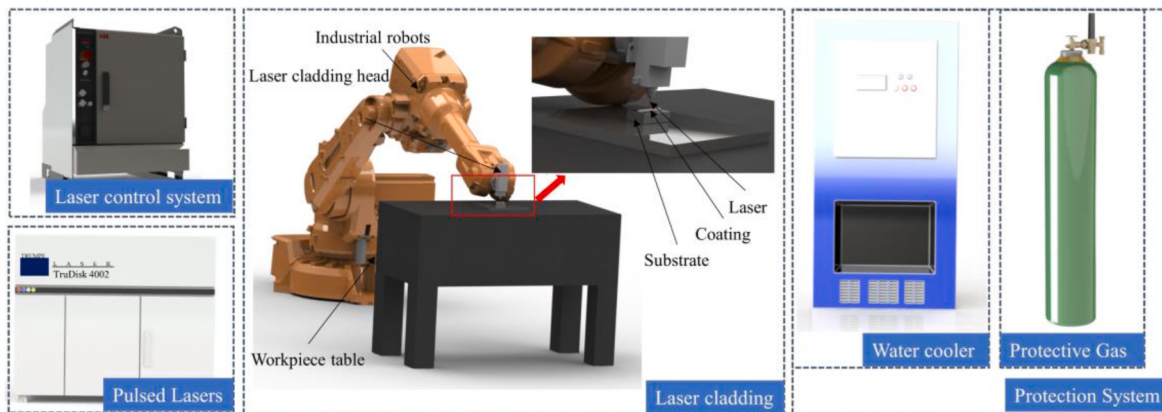
¹ These authors contributed equally to this work and should be considered co-first authors



Table 1

Elemental composition (wt.%) of the AISI 1045 steel substrate.

Element	C	Si	Mn	Cr	Ni	Cu	Fe
Component	0.42–0.50	0.17–0.37	0.50–0.80	≤0.25	≤0.30	≤0.25	Rest

**Fig. 1.** Schematic diagram of laser cladding system.**Table 2**

Phase formation criterion parameters.

alloy	δ	VEC	$\Delta H_{mix}(\text{kJ}\cdot\text{mol}^{-1})$	$\Delta S_{mix}(J\cdot(K\cdot\text{mol})^{-1})$	Ω	$\Delta \chi$	γ	$\Lambda(J/(mol\cdot K))$
TM40	5.251	7.4	-16.32	13.860	1.370	0.154	1.162	0.503
TM31	5.100	7.5	-13.52	14.317	1.757	0.166	1.162	0.550
TM22	4.944	7.6	-10.64	14.534	2.331	0.171	1.162	0.595
TM13	4.779	7.7	-7.68	14.317	3.270	0.169	1.1624	0.627
TM04	4.607	7.8	-4.64	13.860	5.380	0.161	1.1624	0.653

Mo_x ($x = 0, 0.25, 0.5, 0.75$, and 1) high-entropy-alloy coating was prepared by changing Ti and Mo content. The formation and properties of the coating were predicted by the first-principles calculation. Besides, the changing rules of the coating's microstructure and properties were analyzed through experiments.

2. Experiment

2.1. Coating preparation

Simple substances Co, Cr, Fe, Ni, Ti, and Mo powders (size 45–108 μm) with a purity of more than 99.9 % were used as raw materials in the work. Ball-mill mixing was performed according to the atomic ratio of $\text{CoCrFeNiTi}_{1-(1-x)}\text{Mo}_x$ ($x = 0, 0.25, 0.5, 0.75$, and 1). The coatings were named TM40, TM13, TM22, TM31, and TM04. The speed was 300 r/min, with the ball-milling time of 15 h and a ball-material ratio of 1 : 7. Steel AISI 1045 was used as the substrate for the test. Table 1 lists the chemical composition of the AISI 1045 steel substrate. The substrates were polished before powder presetting. Subsequently, they were cleaned with ethanol to ensure a dry and pristine surface. The parameters of this experiment are laser power 1650 W, scanning speed 10 mm/s and spot diameter 3 mm.

Fig. 1 illustrates the laser cladding consisting of a pulsed laser (TruDisk 4002 (6 C), TRUMPF, Germany), a laser-pulse waveform control system (IRC5 Single, ABB Engineering, China), a laser coating head (BW330WF020, Raytool, China), an industrial robot (IRB2600, ABB Engineering, China), and a laser water cooler (XH-05BDS, Xuehai, China). Argon (Ar) is selected as the protective gas during the laser coating.

2.2. Characterization

The sample was cut into a size of $10 \times 10 \times 5$ mm to analyze the laser cladding $\text{CoCrFeNiTi}_{1-(1-x)}\text{Mo}_x$ high-entropy-alloy coating. The mixed solution (HCl: $\text{HNO}_3 = 3 : 1$) was dropped on the coating surface for 10–60 s. Then, the sample was placed in an alcohol solution after corrosion. Ultrasonic cleaning was used to remove dirt on the surface for analysis. Scanning electron microscopy (High-Technologies TM3030Plus, Hitachi, Japan) was used to measure the morphology of the cladding. Besides, an energy spectrometer (Model 550i, IXRF, USA) was used to test the composition and distribution of elements.

The performance tests of the coating included microhardness, nano-indentation, frictional wear, and corrosion resistance. A microhardness tester (MVA-402TS, HDNS, China) was utilized to measure the microhardness of the coating at the 500-g pressure for 10 s. The wear resistance of the coating was measured using a friction wear testing machine (HSR-2M, ZHKh, China). The friction ball was Si_3N_4 , with the loading force of 30 N, reciprocating wear for 30 min, and a reciprocating length of 3 mm. A nanoindenter (Hysitron TI Premier, Hysitron, America) was used for the nano-indentation test. Loading force was set to 2,000 μN , and the durations for the loading, holding, and unloading were 10, 5, and 10 s, respectively. The coating's corrosion resistance was tested using a potentiometer (Chi760e, Chinstrc, China) at -1.5 – 1.5 V in a 3.5 % NaCl solution.

The prepared coating was ground to flat, and then the ground coating was cut into a rectangular sample piece of $8 \times 3 \times 5$ mm. Then, the sample piece was polished and subjected to an XRD test using the X-Pert Pro MPD instrument from the Netherlands with a parameter setting of 40 kV. $\text{Cu K}\alpha$ radiation measurement ($\lambda = 0.15418$ nm) was performed at 20 mA, with 20 of 10–90°, the scanning step size of 0.05°, and the

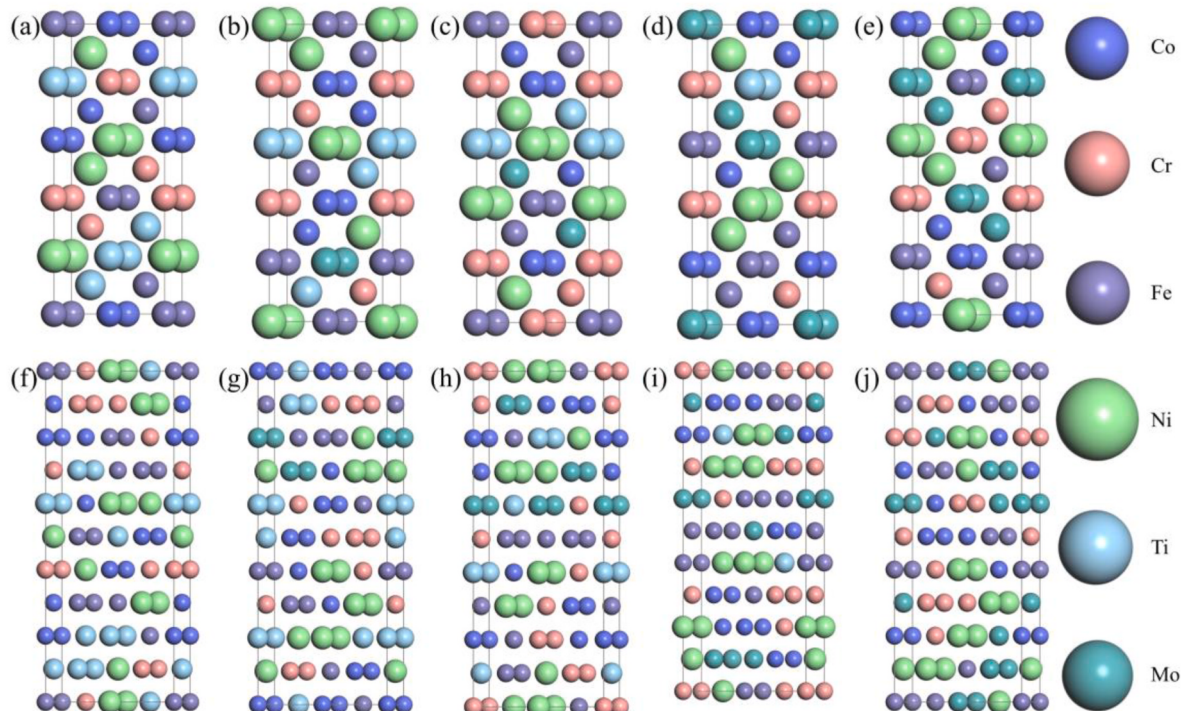


Fig. 2. Supercell structure: (a)–(e) CoCrFeNiTi_(1-x)Mo_x BCC phase, (d)–(e) CoCrFeNiTi_(1-x)Mo_x FCC phase.

Table 3
Geometry Optimization result and E_c of different x added.

Alloy	Density(g/cm ³)		E _a (eV)		E _c (eV/atom)	
	BCC	FCC	BCC	FCC	BCC	FCC
TM40	7.6694	7.6258	-29335.1000	-58670.4000	-4.2247	-3.9084
TM31	7.9877	7.9712	-29668.3921	-59337.3067	-4.7443	-4.0077
TM22	8.3666	8.3666	-30002.4544	-60002.9166	-4.5166	-4.2301
TM13	8.6751	8.6600	-30334.5734	-60669.7658	-4.6650	-4.1690
TM04	9.0139	8.9997	-30667.7322	-61335.7414	-4.3583	-3.9596

Table 4

Calculation of elastic constants of high entropy alloys.

Alloy	C_{11}		C_{12}		C_{44}	
	BCC	FCC	BCC	FCC	BCC	FCC
TM40	350.0066	256.6644	159.2173	183.0776	93.2641	115.8374
TM31	353.2594	280.9019	169.9708	185.2742	102.2915	126.3727
TM22	364.5022	276.5320	169.6003	196.9630	130.0527	114.6004
TM13	353.2594	351.1520	169.9708	207.4704	102.2915	135.7256
TM04	375.7605	314.6092	183.1283	206.1083	118.9184	143.0454

Table 5

Calculation results of material properties of high entropy alloys.

Alloy	Bulk modulus B(GPa)	Shear modulus G(GPa)	B/G	Young modulus E(GPa)	Poisson ratio(ν)	Hardness (GPa)
TM40	BCC	218.2330	86.4079	2.5256	229.0000	0.3251
	FCC	207.4894	72.7337	2.8527	195.3724	0.3431
TM31	BCC	228.7113	86.2467	2.6518	229.8482	0.3325
	FCC	217.0957	85.3457	2.5437	226.3720	0.3262
TM22	BCC	234.3427	99.6484	2.3517	261.8325	0.3138
	FCC	223.4226	80.8984	2.7618	216.5576	0.3385
TM13	BCC	237.1897	98.2388	2.4144	258.9641	0.3180
	FCC	251.1820	99.3417	2.5285	263.3121	0.3253
TM04	BCC	247.2909	98.8652	2.5013	261.7180	0.3236
	FCC	242.1834	96.6060	2.5069	255.8049	0.3240

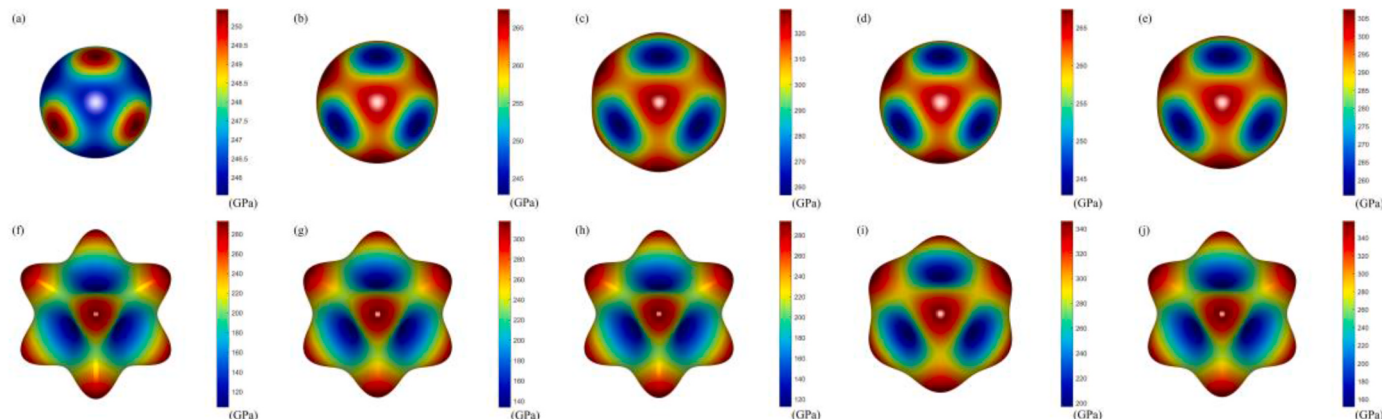


Fig. 3. Anisotropy of Young's modulus of high entropy alloys:
(a)–(e) CoCrFeNiTi_{1-(1-x)}Mo_x (x = 0, 0.25, 0.5, 0.75, 1) BCC phase
(f)–(j) CoCrFeNiTi_{1-(1-x)}Mo_x (x = 0, 0.25, 0.5, 0.75, 1) FCC phase.

measuring time of 10 s for each step.

3. Results and discussion

3.1. Theoretical calculations

The high-entropy alloy coating is not composed of single random solid-solution phases. Intermetallic compounds, nano-phases, and amorphous phases exist. The phase compositions in the coating significantly affect coating performance. The phase compositions of the CoCrFeNiTi_{1-(1-x)}Mo_x high-entropy alloy are evaluated by calculating the mean square difference of atomic radius difference δ , valence electron concentration VEC , mixing enthalpy ΔH_{mix} , mixing entropy ΔS_{mix} , entropy-enthalpy ratio Ω , electro-negativity difference $\Delta\chi$, atomic size difference γ , and Λ [11,12].

Table 2 presents the calculations. The alloy forms random solid-solution phases [13] with $\Omega > 1.1$, $1 < \delta < 6.6$, and ΔH_{mix} between -20 and 5 kJ·mol⁻¹. It also forms solid solution phases [14] when $\gamma < 1.175$. Five coatings can form random solid solutions when they meet the above conditions. Besides, the valence electron concentration (VEC)

serves as a reliable indicator for determining the specific structure of the solid solution. It is easy to form BCC phases when $VEC \leq 6.87$. FCC and BCC phases exist when $6.87 \leq VEC \leq 8$. FCC phases form when $8 \leq VEC$.

The VEC of the five coatings is between 6.87 and 8, so FCC and BCC phases exist. It can be determined whether there is an intermetallic compound (IMC) generation by electro-negativity differences $\Delta\chi$ and Λ . IMC is formed when $\Lambda < 0.24$; the system is composed of a random solid solution and IMC when $0.24 < \Lambda < 0.96$; the system is composed of a random solid solution when $0.96 < \Lambda$; IMC is easy to form [15,16] when $\Delta\chi > 0.133$. Λ of five coatings is between 0.24 and 0.96, and $\Delta\chi$ is greater than 0.133, indicating that IMC exists in five coatings. IMCs are prone to form due to the low enthalpy of mixing Ti with Ni, Co, etc.

The automation toolkit ATAT is used to construct a random single-phase CoCrFeNiTi_{1-(1-x)}Mo_x high-entropy-alloy solid solution after a specific random structure method under the alloy theory. The models of high-entropy-alloy solid solutions use $1 \times 2 \times 5$ supercells. They are a body-centered cubic (BCC) supercell structure of 20 atoms and a face-centered cubic (FCC) supercell structure of 40 atoms. Fig. 2 shows the supercell structure of the CoCrFeNiTi_{1-(1-x)}Mo_x high-entropy alloy.

The generalized gradient approximation (GGA-PBE) method was

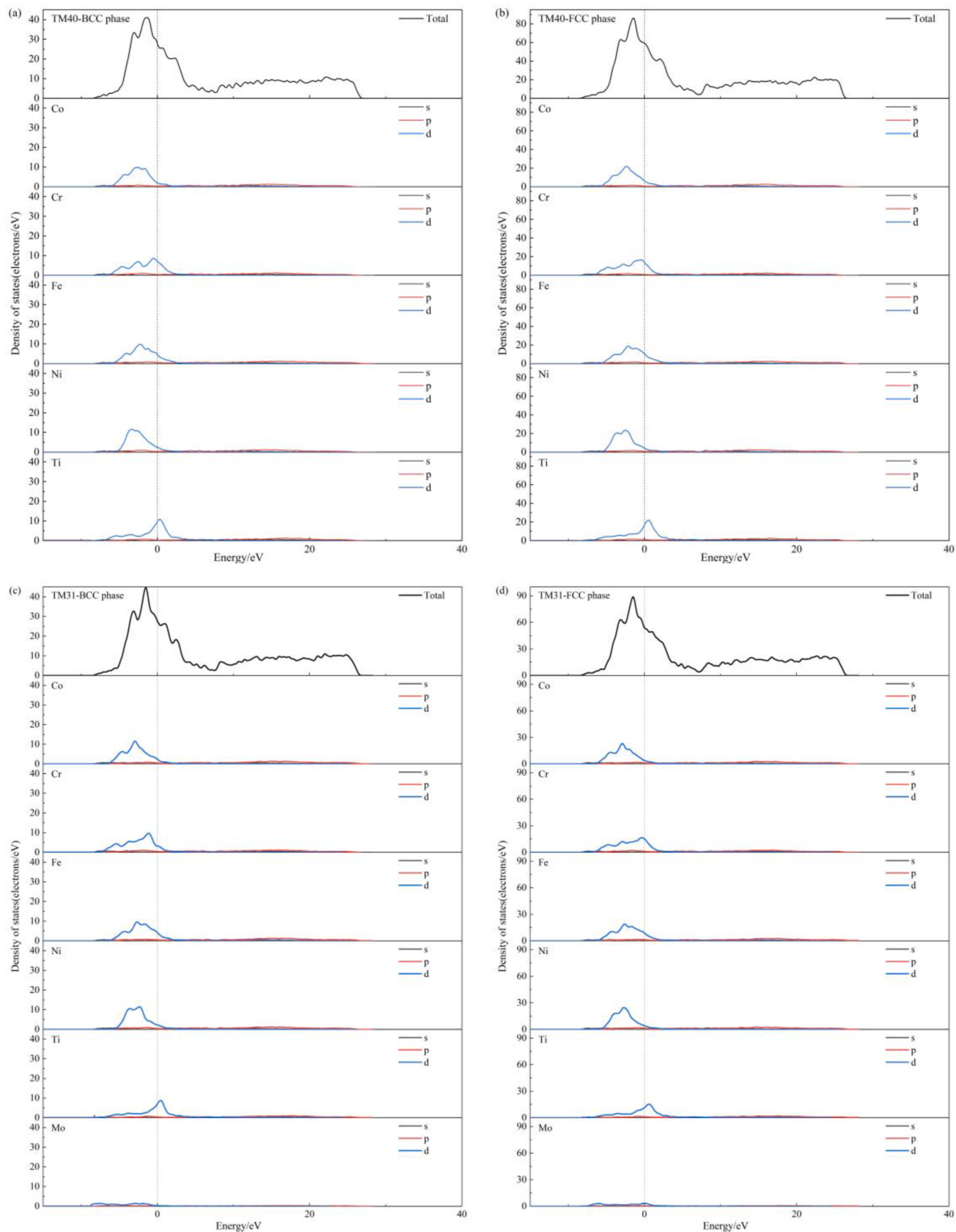


Fig. 4. Density of states diagram for different high entropy alloys.

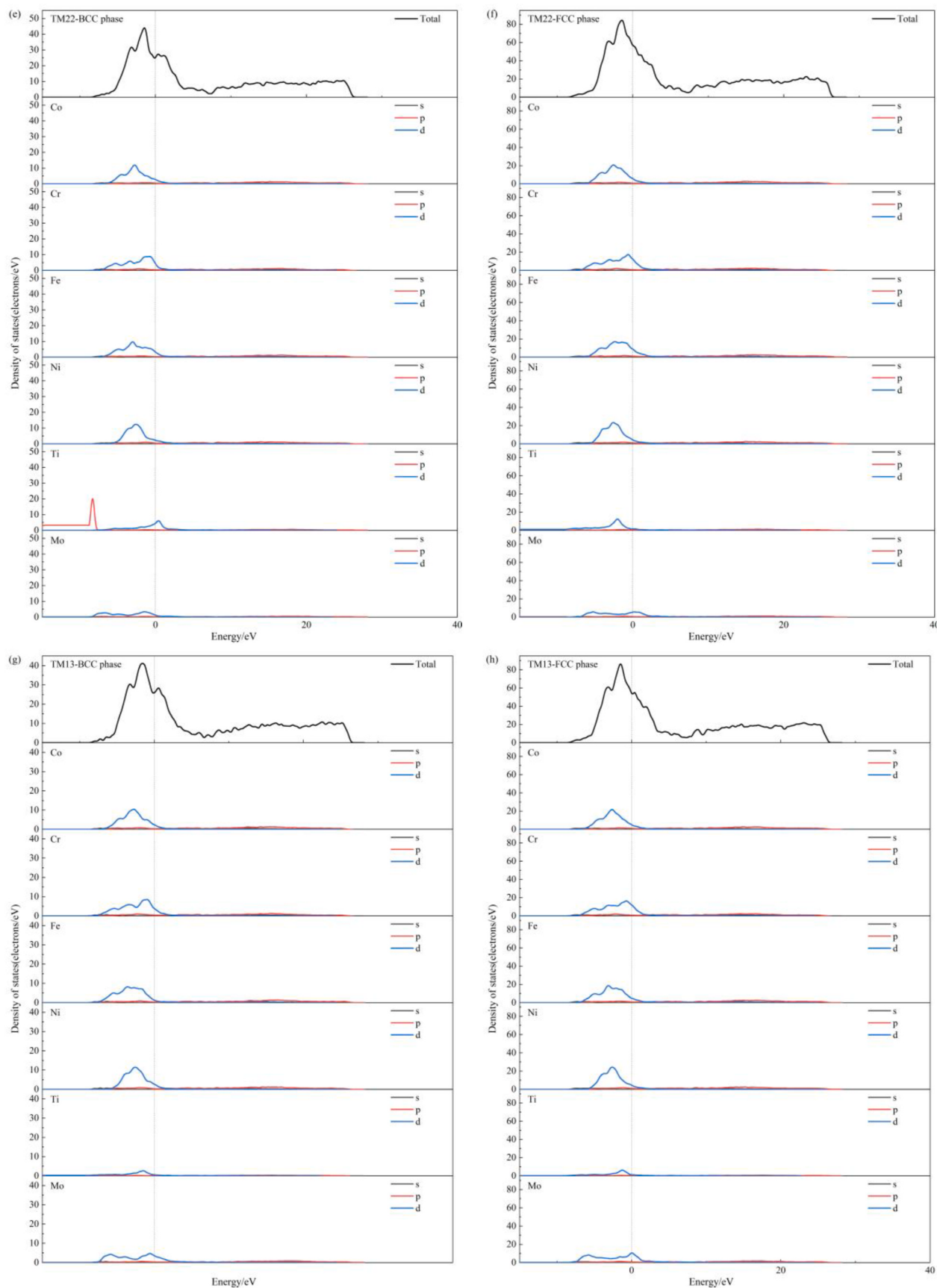


Fig. 4. (continued).

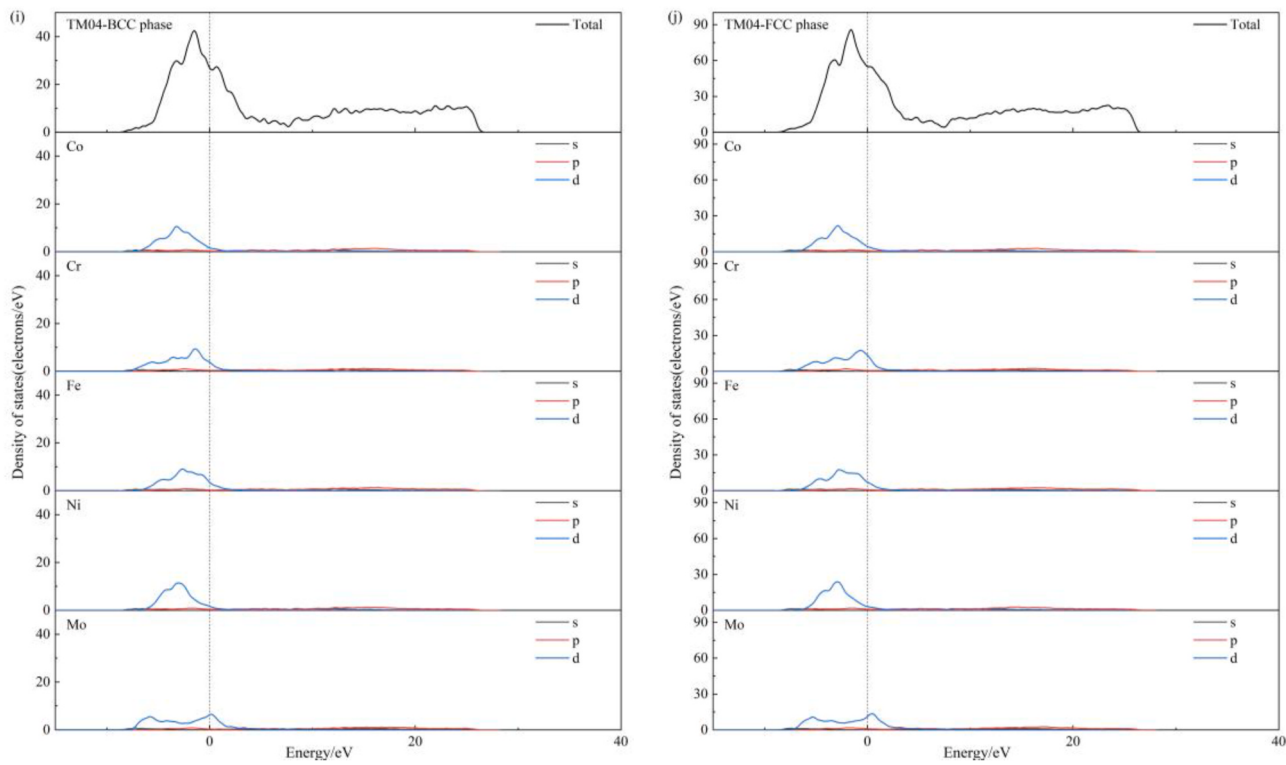


Fig. 4. (continued).

adopted for calculation using the CASTEP module. Energy cutoff was 400 eV, with the k -point of $10 \times 5 \times 2$, the total-energy deviation convergence of 2.0E-5eV/atom during the optimization, the maximum atomic force of 0.1 eV/Å, the stress deviation less than 0.1 GPa, and the maximum displacement of 0.01 Å. The structure optimization was calculated using the BFGS method. First, geometry optimization was performed on the established super-cell structure, and the energy of each element was calculated. Then, elastic constants and material properties were calculated.

The structure of the established FCC-phase CoCrFeNiTi supercell ($1 \times 2 \times 5$) is optimized to verify calculation accuracy. Different lattice constants are obtained as follows: $a = 3.630684$ Å (3.606 Å [17] and 3.6001 Å [18]), $b = 7.161062$ Å, and $c = 18.319885$ Å. The error rates are 0.6799 and 0.8424 %, respectively, indicating that the calculation parameters meet the theoretical expectations.

Geometry optimization and total-energy calculation are performed on supercells, and each atomic energy is calculated. Cohesive-energy Eq. (1) [19] is used to determine the structural stability of the BCC and FCC phases from energy. Table 3 lists the geometry optimization and cohesive energy. The density of the alloy gradually increases with increased x . Lower cohesive energy means better structural stability. The cohesion energy of all alloys is less than -3 , so the structure is stable. The cohesive energy of the BCC phase is smaller than that of the FCC phase in five alloys, indicating that the BCC phase is more stable. BCC-phase generation is the highest among the five high-entropy-alloy coatings in the solid solution with BCC and FCC phases.

$$E_c = \frac{1}{n} \left(E_n - \sum \alpha E_{atom} \right) \quad (1)$$

where E_c is cohesive energy; E_n is total energy; E_{atom} is single-atom energy; n is the total number of atoms; α is the atom number of each element.

The elastic constant, a physical quantity that characterizes the elasticity of a material, directly affects material performance. The partial equality relation is achieved between the elastic constants, that is,

$C_{11}=C_{22}=C_{33}$, $C_{44}=C_{55}=C_{66}$, and $C_{12}=C_{23}=C_{13}$. Therefore, three independent elastic constants can be obtained by evaluating the mean value [20]. Table 4 lists the calculation results. The mechanical stability of the cubic structure can be judged according to the elastic constant. Eq. (2) shows the reasons for judgment. The above ten phases exhibit mechanical stability by considering the calculation results.

$$\begin{cases} C_{44} > 0 \\ C_{11} > |C_{12}| \\ C_{11} + 2C_{12} > 0 \end{cases} \quad (2)$$

The Voigt-Reuss-Hill approximation can be used to calculate the bulk modulus (B), shear modulus (G), Young's modulus (E), Poisson's ratio (ν), and theoretical hardness of high-entropy alloys. Table 5 lists the calculation results. The material exhibits brittleness when B/G is less than 1.75 and the Poisson's ratio is greater than 0.26 according to the empirical formula. The B/G of the five coatings are all greater than 2, and the Poisson's ratio is greater than 0.3, so they exhibit toughness through comprehensive calculations. The BCC phase has a higher hardness than the FCC phase in terms of theoretical hardness. Coating TM22 is harder, while coating TM40 is less hard by considering cohesive energy and phase composition.

Young's modulus is used to characterize the anisotropy of high-entropy alloys (Fig. 3). The more irregular the spherical shape in the anisotropy, the stronger the anisotropy. BCC and FCC phases of TM22 are the most irregular, indicating that TM22 has a high anisotropy from Fig. 3 (c) and (h). The high-entropy-alloy coatings studied have higher strength in the direction of [1 1 1], [1 1 1], and [-1 1 1]. The variation in Young's modulus is consistent with the calculated anisotropic indices presented in Table 5 and Fig. 3.

The electronic structure of a compound is related to the properties of the material. The electron distribution can be obtained in the material in a certain energy range by calculating the state density and the partial state density of high-entropy alloys. Then, the inherent changing rule of material performance can be elucidated. Fig. 4 shows the state density of its ten supercells. The state density of the high-entropy alloy is non-zero,

Table 6
Population analysis of different high entropy alloys.

Alloy		species	Ion	s	p	d	total	charge(e)
TM40	BCC	Ti	1	2.49	6.41	2.62	11.52	0.48
		Ti	2	2.35	6.41	2.65	11.41	0.59
		Ti	3	2.24	6.37	2.64	11.24	0.76
		Ti	4	2.41	6.36	2.63	11.4	0.6
	FCC	Ti	1	2.33	6.6	2.68	11.6	0.4
		Ti	2	2.39	6.5	2.65	11.55	0.45
		Ti	3	2.31	6.69	2.65	11.65	0.35
		Ti	4	2.45	6.42	2.61	11.47	0.53
TM31	BCC	Ti	5	2.45	6.58	2.64	11.67	0.33
		Ti	6	2.53	6.51	2.61	11.65	0.35
		Ti	7	2.49	6.33	2.63	11.45	0.55
		Ti	8	2.35	6.55	2.63	11.52	0.48
	FCC	Ti	1	2.34	6.45	2.63	11.42	0.58
		Ti	2	2.43	6.47	2.62	11.51	0.49
		Ti	3	2.42	6.47	2.63	11.51	0.49
		Mo	1	2.64	6.19	4.99	13.82	0.18
TM22	BCC	Ti	1	2.37	6.42	2.66	11.45	0.55
		Ti	2	2.32	6.51	2.62	11.46	0.54
		Ti	3	2.36	6.46	2.62	11.44	0.56
		Ti	4	2.33	6.49	2.61	11.42	0.58
	FCC	Ti	5	2.42	6.49	2.64	11.55	0.45
		Ti	6	2.42	6.5	2.61	11.52	0.48
		Mo	1	2.62	6.28	5	13.9	0.1
		Mo	2	2.57	6.07	4.99	13.63	0.37
TM13	BCC	Ti	1	2.36	6.58	2.64	11.57	0.43
		Ti	2	2.39	6.53	2.64	11.55	0.45
		Mo	1	2.69	6.09	4.95	13.74	0.26
		Mo	2	2.6	6.18	5.01	13.79	0.21
	FCC	Ti	1	2.49	6.63	2.63	11.75	0.25
		Ti	2	2.45	6.25	2.64	11.35	0.65
		Ti	3	2.4	6.64	2.62	11.66	0.34
		Ti	4	2.45	6.27	2.62	11.35	0.65
TM04	BCC	Mo	1	2.62	6.07	4.99	13.68	0.32
		Mo	2	2.46	6.47	5.01	13.94	0.06
		Mo	3	2.55	6.4	5.04	13.99	0.01
		Mo	4	2.53	6.36	5.02	13.91	0.09
	FCC	Ti	1	2.24	6.49	2.65	11.37	0.63
		Ti	2	2.69	6.13	4.95	13.77	0.23
		Mo	2	2.56	6.19	4.97	13.72	0.28
		Mo	3	2.43	6.3	5.03	13.76	0.24

exhibiting metallic character at the Fermi level (Energy = 0).

The state density contributed by Mo at the Fermi level increases and Ti decreases with increased x from each state-density map. It is consistent with the changing law of elements. The state density is mainly contributed by the 3d orbitals of Co, Cr, Fe, Ni, Ti, and Mo at the Fermi level. The overall state density is composed of the state density of each element and distributed according to the added proportion. Therefore, $\text{CoCrFeNiTi}_{(1-x)}\text{Mo}_x$ high-entropy-alloy covalent bond is generated.

The state density determines whether the alloying elements can form bonds. The population analysis is employed to assess the atom's ability to gain and lose electrons for alloying elements (Table 6). The ability of

Mo to gain and lose electrons is weaker than that of Ti in a single alloy with Mo and Ti by comparing the abilities of coatings TM40 and TM04. The alloy exhibits better stability in electrochemical corrosion. Therefore, Mo addition improves the corrosion resistance of the coating better than that of Ti when a single element is added.

The ability of single Ti and Mo to gain and lose electrons increases with increased x (the more Mo, the less Ti) whether it is the BCC phase or the FCC phase. Single Ti and Mo have the strongest ability to gain and lose electrons in coating TM13. The electronic stability of TM13 is the poorest and it exhibits higher susceptibility to electrochemical corrosion compared to TM31, TM22, and TM13. Ti content decreases and the coating becomes less corrosion-resistant with increased Mo content. In summary, the corrosion resistance of high-entropy-alloy coatings is higher with Mo addition.

3.2. Forming quality

Fig. 5 shows the molding of the high-entropy-alloy coating. Pores decrease in the coating with decreased Ti content and increased Mo content (Fig. 5 (a), (b), and (d)). TM40 and TM31 exhibit obvious pores; small pores exist in TM13; TM22 and TM04 have no obvious pores. Ti is active and reacts violently with other elements such as C, H, O, and N at high temperatures [21]. The violent reaction causes the molten pool to fluctuate during solidification, and some gases cannot overflow in time. Therefore, they remain in the molten pool, and pores form.

The width of the coating increases while the height decreases with increased x content from the morphology of the coating in Fig. 5(a)–(e). TM22 exhibits an arc shape with a suitable height-width ratio when $x = 0.5$ (Fig. 5 (c)). High Ti content in the violent reaction leads to a taller and narrower molten pool. Besides, laser cladding involves rapid cooling, heating, and fast solidification rates. Therefore, the molten pool solidifies quickly during fluctuations, which makes the coating higher. However, the reaction becomes mild, and the molten pool tends to flow on two sides with increased Mo content. Therefore, the coating is flat with a significantly increased width and a significantly reduced height.

3.3. XRD

Fig. 6 illustrates the XRD spectrum of the $\text{CoCrFeNiTi}_{(1-x)}\text{Mo}_x$ high-entropy alloy. Five coatings all exhibit the FCC phase, BCC phase, and IMCs, which is consistent with the previous phase-composition determination (Fig. 6(a)). The FCC phase in the coating is the γ' phase, and the BCC phase is a disordered solid solution, with the σ phase in the coating. IMCs are CoTi_2 and Co_2Mo_3 , respectively. The peak of the BCC phase of the five coatings exceeds that of the FCC phase, indicating a higher generation rate of the BCC phase. It is consistent with the conclusion of judging the stability of phases by cohesive energy. The XRD diffraction peak changes from a single peak to a multi-peak with increased x . Therefore, Mo content increases and Ti content decreases with increased x . Then, new BCC and FCC phases appear.

The peaks of the single-peak BCC phases decrease and move at a large angle with increased x when 2θ is $43\text{--}45^\circ$ (Fig. 6 (b)). The decreased peak indicates that its content is reduced in the coating. The highest peak deflects at a large angle, so the lattice constant is changed. Mo content increases and Ti content decreases due to increased x , which changes the effect of the lattice distortion [22]. Then, the lattice constant becomes smaller, so the highest peak deflects at a large angle. Ti addition can induce a phase transition from FCC to BCC. Therefore, when Ti content decreases, its BCC peak decreases. The peak of the σ phase increases and deflects at a small angle, indicating increased content and lattice constant when 2θ is 50° . Besides, the atomic sizes of Ti and Mo are large, and the coating's lattice distortion effect is subtle when the ratio of Ti to Mo is small. Therefore, the lattice distortion effect becomes greater when the ratio of Ti to Mo reaches 1 : 1 in the coating.

The peaks of the FCC and σ phase increase with increased x between 50 and 53° and reach the maximum when $x = 0.75$ (Fig. 6 (c)). The

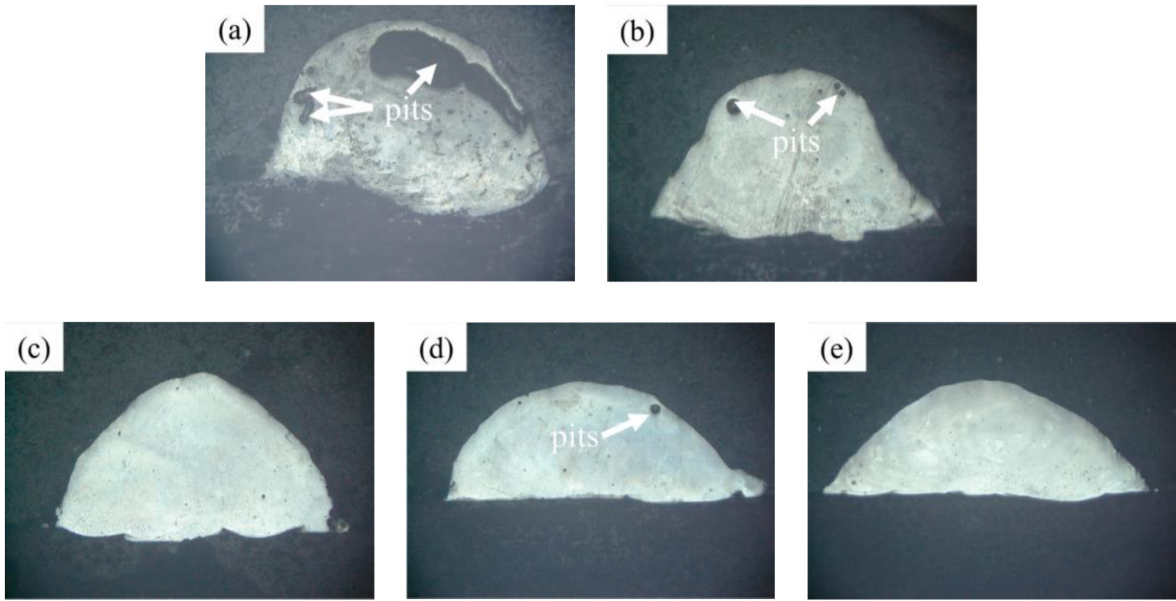


Fig. 5. Forming quality of high entropy alloys with different x ratios.

content of the FCC and σ phase increases corresponding to the peak in TM13. On the one hand, decreased Ti content reduces FCC content in the coating. On the other hand, Mo addition helps to induce the generation of the σ phase. The peak deflects at a small angle and then at a large angle with increased x . Therefore, the lattice constant increases first and then decreases and reaches its maximum in TM22 alloy. The width of the diffraction peak decreases with increased x , indicating that the grain size of the FCC and σ phase decreases (Fig. 6 (c)).

The peak of CoTi_2 increases gradually with increased x , indicating increased CoTi_2 content in the coating. The peak of CoTi_2 initially decreases and then increases with increased x . At $x = 0.25$, the width of the CoTi_2 peak is the smallest. The lattice constant of CoTi_2 is the largest in TM31. The width of the diffraction peak of CoTi_2 is the largest in TM31, indicating a larger grain size. The Co_2Mo_3 phase appeared in TM04 exclusively. Mo is not significantly segregated when Ti exists in the coating.

3.4. Microstructure

Fig. 7 illustrates the microstructure of different high-entropy alloys. TM40 exhibits a typical cellular crystal, and spherical phases exist in the coating (Fig. 7(a)). The coating exhibits obvious dendrites and spherical phases exist (Fig. 7(b)–(d)). The dendrites of TM31 are thick and large. Besides, dendrites become finer with more Mo, which is consistent with the grain-size change in the XRD conclusion therefore. The spherical phase becomes a heterogeneous nucleation due to the large spherical phase. Besides, the surrounding dendrites are distributed around the spherical phase, and then a petal-like interface forms (Fig. 7 (b)). TM04 exhibits typical dendrites and cellular crystals, and spherical phases exist in the coating (Fig. 7 (e)).

Dot testing and element surface scanning were performed on the microstructure in Fig. 7 to explore the element distribution. Table 7 and Fig. 8 present the results. The ratio of Ti concentration to the sum of Co, Fe, and Ni concentration is close to 2 : 1 (P1, P4, P7, and P10 in Table 7) in the spherical phases of TM40, TM31, TM22, and TM13 (Table 7). The spherical phase is the CoTi_2 phase from the XRD map. Fe and Ni in the lattice replace Co since Co, Fe, and Ni have the same atomic radius, which makes IMCs in the coating exhibit CoTi_2 phases [23]. Ti has obvious segregation (Fig. 8(a)–(d)). There is a convergence of Co, Fe,

and Ni in the segregating point, but the segregation effect is not as obvious as Ti.

The EDS results in Fig. 7 show that Ti content at points P2, P5, P8, and P11 is higher than that at points P3, P6, P9, and P12. Moreover, Mo at points P5, P8, P11, and P14 are higher than that at points P6, P9, P12, and P15. Combined with the XRD results, P2, P5, P8, P11, and P14 belong to the BCC phase; P3, P6, P9, P12, and P15 belong to the FCC phase. Dot testing was performed on grain boundaries and interfaces in the coating, and the proportion of Mo is significantly greater than doped content. The segregation of Ti in the spherical phase reduces Ti content in the coating. Co, Fe, and Ni converge on the spherical phase when the coating forms the CoTi_2 phase. Then, the proportions of Co, Fe, and Ni at the grain boundary and interface decrease, while Mo content increases. Meanwhile, when generating the BCC phase, it is easy to precipitate the σ phase making the Mo element content higher.

The content of the spherical phase in the coating increases with increased x (Fig. 7(a)–(d)). The spherical phase is at most in TM31, which is consistent with the conclusion of XRD that a larger grain size leads to a broader CoTi_2 diffraction peak. The concentration ratio of Mo and Co in TM04 is close to 3 : 2 from point P13 in Table 7. The spherical phase is Co_2Mo_3 from the XRD spectrum. Dot testing is performed on grain boundaries and interfaces in TM04. There is no obvious difference in the proportion of elements, indicating that the elements are evenly distributed in the coating from the test results of points P13–15. Therefore, elements are evenly distributed (Fig. 7 (e)).

3.5. Microhardness

Fig. 9 shows the microhardness of different coatings. Fig. 9 (a) illustrates microhardness and Fig. 9 (b) presents average microhardness. The microhardness curve of TM22 is significantly higher than that of other coatings, with an average of more than 700 HV_{0.5} (Fig. 9 (a)). The average hardness of TM22 is the highest, at 873.28 HV_{0.5} (Fig. 9 (b)), which is consistent with the theoretical hardness and anisotropic results. The FCC and BCC phases have large lattice distortion in TM22, which makes a harder high-entropy-alloy coating [24] from the XRD results mentioned. Therefore, the overall microhardness of TM22 is higher. Hardness significantly decreases between the dilution zone and the coating; however, the hardness of the dilution zone is similar to that of

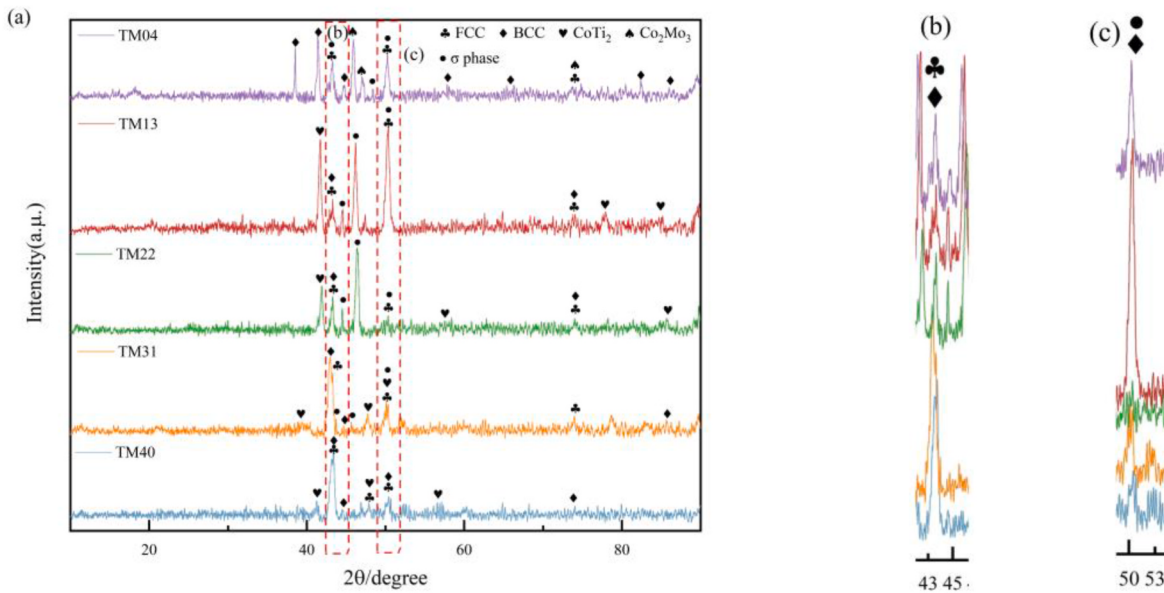


Fig. 6. XRD pattern of different coatings.

the substrate. The substrate is melted, and a large amount of Fe is doped into the dilution zone under a high-energy laser beam. The proportion of Fe is higher in the dilution zone, which significantly reduces the lattice-distortion effect of the dilution zone.

The average hardness of the coating tends to increase first and then decrease with increased x (Fig. (b)). The average hardness of TM22 reaches a maximum (873.28 HV_{0.5}). The lattice distortion effect is greater with higher hardness, which is consistent with the peak deflection in XRD when the ratio of Ti to Mo is 1 : 1 or $x = 0.5$. When the ratio of Ti to Mo is 1 : 1, the performance characteristics of Ti and Mo can be fully utilized in terms of hardness. Generally, Mo addition improves coating hardness, and the hardness of TM04 is higher than that of TM40. However, the addition of a single element (either Ti or Mo) to the CoCrFeNi high-entropy alloy does not yield a comparable improvement in hardness with Ti and Mo addition.

3.6. Nanoindentation analysis

Eqs. (3)–(6) are used to calculate the mechanical performance parameters obtained in nanoindentation. Table 8 lists the measured and calculated data. Fig. 10 shows the results of the nanoindentation test.

The nanoindentation depth of TM22 is smaller than that of other coatings under the same load with the maximum depth of 59.7082 nm from Fig. 10 and Table 8. TM22 has strong resistance to plastic deformation. Generally, the higher the microhardness, the smaller the nanoindentation. TM22 has high hardness (16.9894 GPa) from Table 7 and the previous microhardness. The TM22 coating has a high local elastic modulus of 265.5606 GPa. The overall hardness of TM40 is lower (12.9352 GPa). Therefore, the nanoindentation depth of TM40 is the deepest (72.6825 nm). The reason for the highest hardness of TM22 is that the TM22 high-entropy-alloy coating has a greater lattice distortion

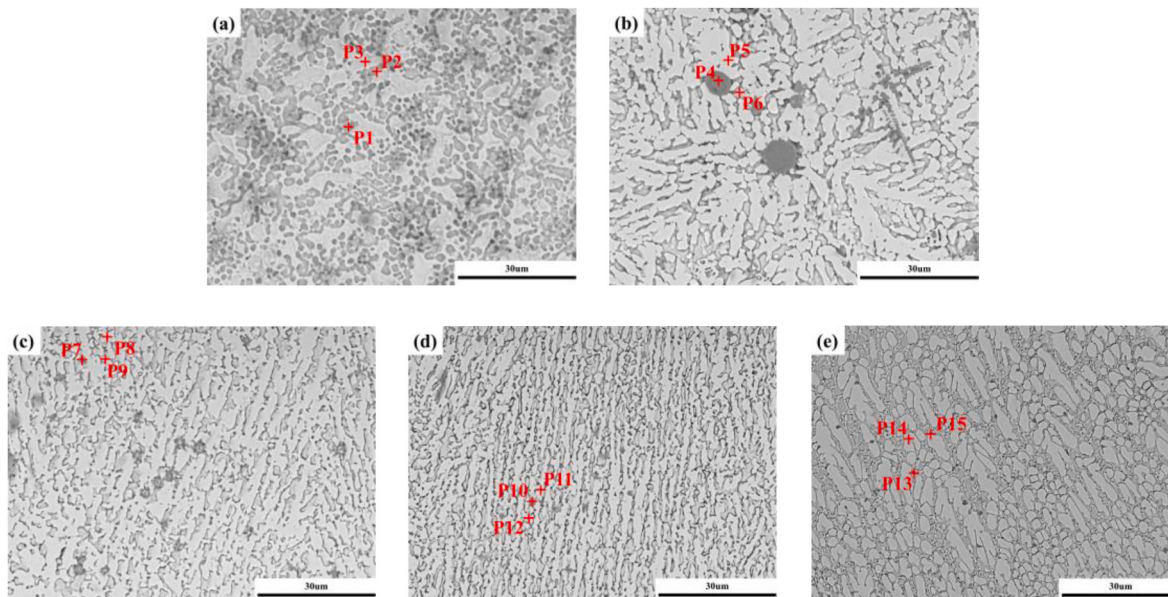


Fig. 7. The microstructures of different coating (a) TM40, (b) TM31, (c) TM22, (d) TM13, (e) TM04.

Table 7

The EDS results of different points in Fig. (at.%).

alloy	Atomic/%					
	Ti	Cr	Fe	Co	Ni	Mo
TM40	P1	54.638	—	20.346	10.582	14.434
	P2	15.334	30.447	26.137	17.557	10.525
	P3	7.286	31.630	24.488	22.127	14.469
TM31	P4	56.406	—	15.667	7.109	16.013
	P5	16.587	15.086	25.945	17.067	11.645
	P6	9.653	27.225	18.582	16.387	17.756
TM22	P7	63.165	—	—	10.893	9.767
	P8	8.636	12.290	16.236	17.714	10.101
	P9	5.680	17.729	24.438	11.813	24.883
TM13	P10	55.996	—	4.847	5.559	6.558
	P11	3.365	18.345	16.323	12.049	9.500
	P12	4.119	13.595	23.370	15.089	16.836
TM04	P13	—	23.125	11.599	15.204	11.113
	P14	—	17.648	12.927	11.595	12.210
	P15	—	18.099	15.815	15.228	14.527
						36.332

effect. Therefore, its resistance to deformation is strong, which is consistent with the rules of microhardness therefore.

The resilience of all coatings decreases first and then increases from the table. TM04 has greater resilience and elastic recovery ability (35.8156 nm), while that of TM22 is weak (28.5833 nm). The elastic modulus reflects the ease of elastic deformation of the coating as well as the binding strength between atoms from a microscopic perspective. TM22 has a high local elastic modulus E and exhibits high elastic contact stiffness S due to the large lattice distortion effect of the coating. TM13 exhibits a high degree of plasticity for energy storage, which enables enhanced energy absorption during loading (Table 8). Therefore, it is less likely to fracture, and the crack resistance of the coating is improved.

$$\delta = h_{max} - h_f \quad (3)$$

$$Q_{total} = Q_e + Q_p \quad (4)$$

$$Q_e = \int_{h_f}^{h_{max}} Pdh \quad (5)$$

$$Q_p = \int_0^{h_f} Pdh \quad (6)$$

where δ is resilience; Q_{total} is total energy; Q_e is elastic deformation energy; Q_p is plastic storage energy; P and h are the pressure applied during the indentation process and the downward displacement of the probe, respectively.

3.7. Tribological performance

The friction and wear of different coatings are tested. Table 9 lists COF and the wear mass loss. Fig. 11 shows the wear morphology and COF curve. TM22 has the lowest COF (0.7026) and wear mass loss (0.0410 mm³). The COF of TM40 is the highest (0.9769) with maximum wear mass loss (0.1250 mm³).

The wear resistance of the coating is related to hardness [25]. In theory, the higher the hardness, the better the wear resistance, and the less the wear mass loss of COF. However, the wear mass loss in TM31 is the highest among all coatings. The CoTi₂ diffraction peak in TM31 becomes wider with increased x from an XRD perspective, indicating a larger grain size. Spherical phase CoTi₂ is larger than other coatings, and the large hard phase is more likely to fall off under pressure during wear from a microstructure perspective. Abrasive particles form in the friction pair, and extensive grinding is conducted on the coating surface. Consequently, the wear mass loss of TM31 exceeds that of TM40 when the COF for TM31 is significantly lower than that for TM40. Grooves are

uniformly distributed across the coating after wear. (Fig. 11 (c)). The hard phase sheds more and has a greater effect on the grinding of the coating. COF is stable at the early wear stage from the COF curve in Fig. 11 (d). Surface roughness decreases significantly, while COF keeps rising in the latter half of the wear process due to the substantial detachment of abrasive particles. The COF of TM22 decreases significantly in the latter half of the friction and wear process, indicating better surface roughness from the COF curve in Fig. 11 (f). There are fewer grooves and pits after wear with the minimum wear mass loss (0.0410 mm³) (Fig. 11 (e)).

The wear forms of high-entropy-alloy coatings are abrasive and adhesive wear with obvious grooves, pits, and scratches from the wear morphology. SEM and EDS inspection is performed for the worn surface (Figs. 12 and 13). The surface scan results show that O is enriched in the bright white and dark areas, these two parts are the most severely oxidized during the wear process. Ti is enriched in some areas. Based on the previous section, the segregation of Ti occurs, which causes enrichment. Dot tests are performed on bright white, dark, and metallic areas (Fig. 13). The RBI test shows that O content in the bright white areas of P1, P4, and P7 exceeds 60 %, and there are fewer other elements. Wear debris is attached to the friction pair during the grinding process. It is re-bonded to the friction surface to form a bright white area in the process of reciprocating wear. Therefore, adhesion wear occurs during friction. The distribution of elements in the metallic areas of P2, P5, and P8 is relatively uniform with less O; therefore, it is judged to be groove. The elements in the P3, P6, and P9 areas are evenly distributed, but O content is high, indicating that they are worn areas.

Fig. 14 illustrates the wear form. The formation of pits is primarily attributed to inherent coating defects and the detachment of the hard phase during wear. Large and deep holes are generally inherent coating defects, while small and shallow holes are caused by the shedding of the hard phase (Fig. 11(a)). Grooves are caused by the grinding of the coating surface by hard-phase particles driven by the friction ball during the friction-pair movement. Meanwhile, scratches and debris occur, which makes the groove darker than the coating. Debris ground by the abrasive particles adheres to the friction ball, which causes adhesion and wear to the coating in the subsequent wear process as the wear progresses.

3.8. Corrosion resistance

The lower free corrosion current density (I_{corr}) and higher free corrosion potential (E_{corr}) indicate better corrosion resistance of the coating according to the electrochemical theory. Table 10 and Fig. 15 present data and curves obtained by electrochemical corrosion, respectively. The self-corrosion-voltage order is as follows: TM04 > TM40 > TM31 > TM22 > TM13 (Table 10 and Fig. 15). The self-corrosion voltage of TM04 is the largest (-0.700 V). The self-corrosion-current order is TM31 < TM04 < TM40 < TM22 < TM13. The self-corrosion current quantifies the coating-corrosion rate after the formation of the passivation layer. Therefore, TM31 has the lowest corrosion rate after forming a passivation layer with a self-corrosion current of 5.387 e-007 A.

The corrosion-resistance order is TM04 > TM40 > TM13 > TM22 > TM31 by combining the self-corrosion voltage and self-corrosion current. TM40, TM31, TM22, and TM13 exhibit obvious passivation areas (Fig. 15). Ti exists in the coating, and Ti alloy is a passivating material. The material is passivated during electrochemical corrosion, so the anode dissolution rate decreases greatly with the increased voltage. Fig. 15 shows specific performance. The curve shows a straight upward trend after TM04 experiences the self-corrosion voltage; however, it slows down after the coating containing Ti experiences the self-corrosion voltage.

The corroded surface is scanned (Fig. 16). Fig. 16 (a) shows that pitting mainly occurs in the second phase. The surface scan results show that Ti is enriched in the second phase. Combined with the previous XRD

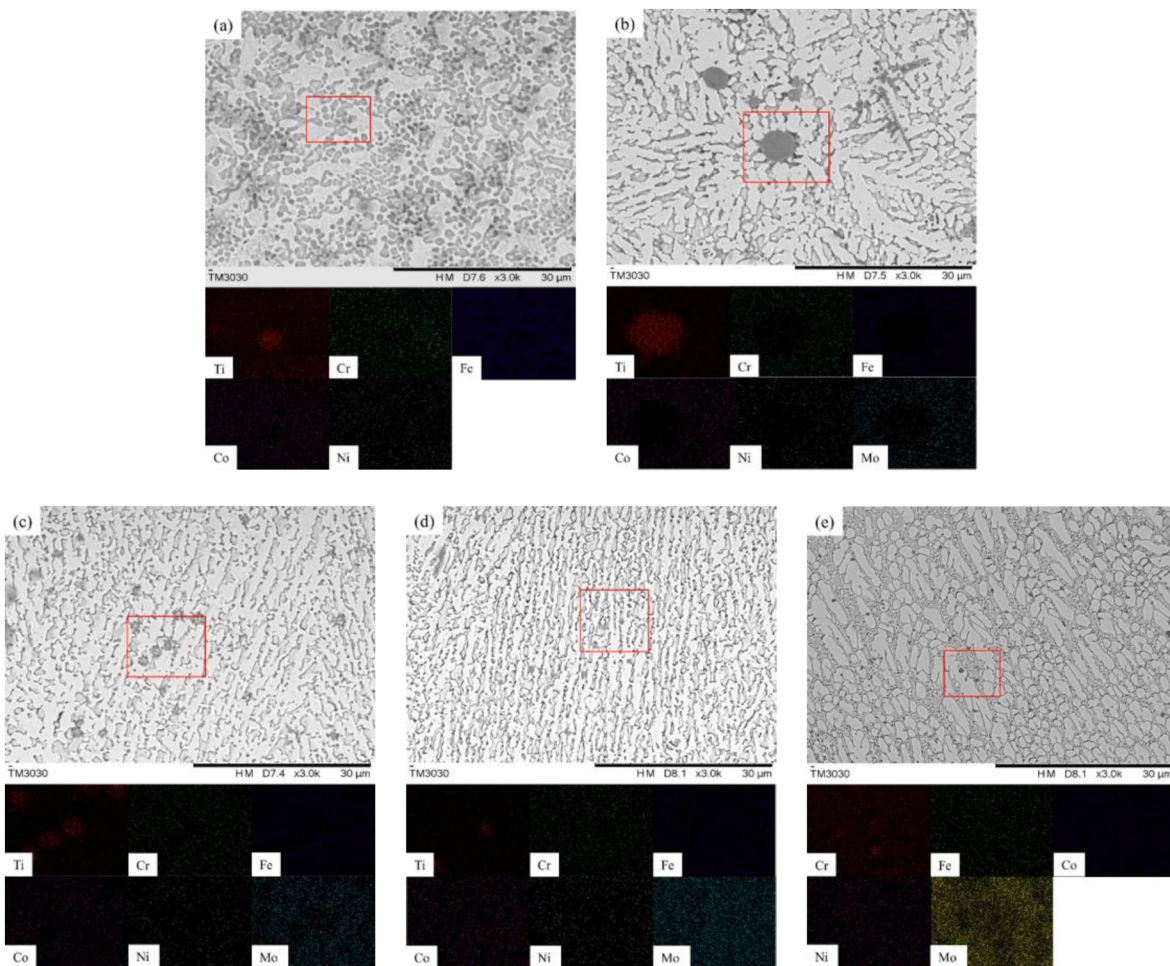


Fig. 8. Elements mapping results of coating:(a) TM40, (b) TM31, (c) TM22, (d) TM13, (e) TM04.

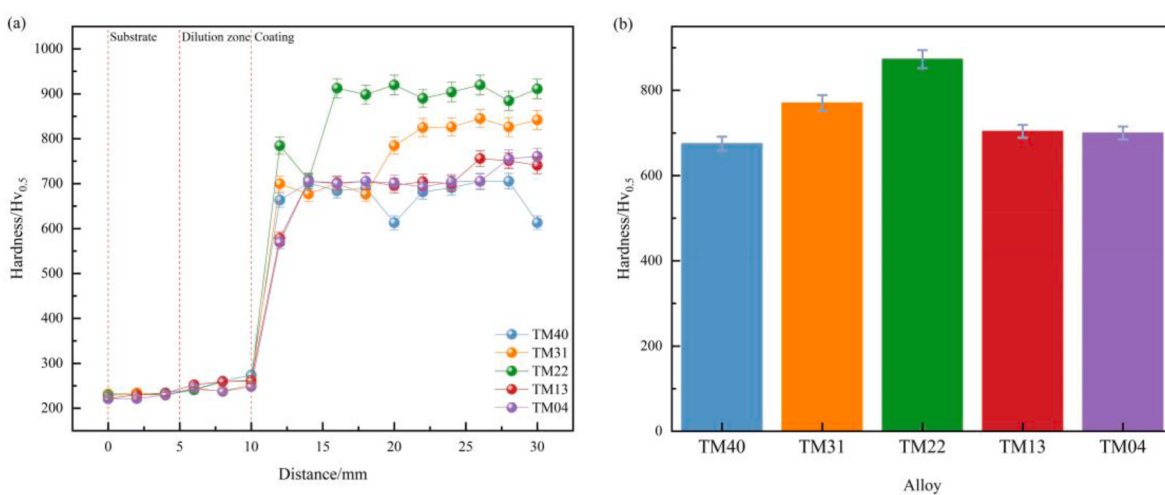


Fig. 9. Microhardness:(a) Microhardness curve (b) Average microhardness.

Table 8

Mechanical characteristic parameters measured by nano-indentation test.

Powder	H _{max} (nm)	H _f (nm)	δ(nm)	E(GPa)	H(GPa)	S(N/nm)	Q _p (10 ⁻¹⁵ J)
TM40	72.6825	38.7306	33.9519	182.3519	12.9352	80.9010	14634.42
TM31	66.0616	32.6593	33.4023	207.0768	15.2415	84.6296	12430.95
TM22	59.7082	31.1250	28.5833	265.5606	16.9894	102.8008	11717.75
TM13	68.3746	37.7457	30.6289	207.6801	14.0720	88.3332	16163.15
TM04	70.8960	35.0804	35.8156	191.0291	13.6833	82.3957	12421.23

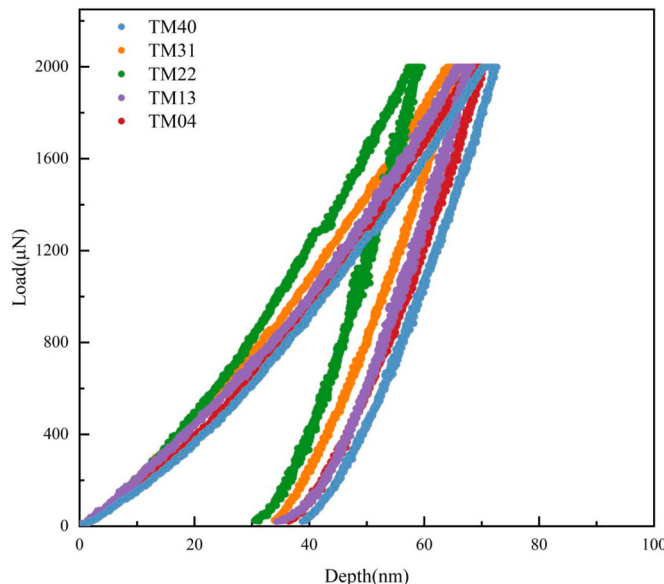


Fig. 10. Displacement-load curves of the nano-indentation test.

Table 9

Wear resistance of coatings with different coating.

alloy	COF	Wear mass loss(mm ³)
TM40	0.9769 ± 0.0192	0.0425 ± 0.0023
TM31	0.8399 ± 0.0492	0.1250 ± 0.0019
TM22	0.7026 ± 0.0253	0.0410 ± 0.0034
TM13	0.7425 ± 0.0249	0.0694 ± 0.0010
TM04	0.7880 ± 0.0325	0.0528 ± 0.0011

and EDS, the phase is IMCs. As x increases, Mo addition causes the coating to gradually change from pitting along the second phase to grain boundary pitting. Pitting occurs near the second phase and at the grain boundary (Fig. 16(b)). An enlarged surface scan of different pitting phenomena is performed, and the second phase pitting is similar to Fig. 16 (a). The element is missing in the grain boundary (Fig. 16 (b2)), proving that it is grain boundary pitting. As x increases, Ti content decreases and Mo content increases, with the gradually decreased pitting of the second phase. Grain boundary pitting is mainly used in the TM13 coating, and no second-phase pitting occurs.

Fig. 17 shows the corrosion mechanism of the CoCrFeNiTi_(1-x)Mo_x high-entropy-alloy coating. OH⁻, H⁺, and H⁻ particles are free from the electrolyte solution and coating surface under energized conditions. The coating consists of a high-entropy alloy susceptible to the galvanic cell reaction. Active metals exhibit a high propensity for electron loss, oxidation, and corrosion. Corrosion resistance is related to the chemical properties of the material, and single Mo exhibits better

corrosion resistance than Ti. Ti is more likely to gain and lose electrons compared to Mo from a micro perspective (see the previous simulation). Electrochemical corrosion is the process of the element gaining and losing electrons. The corrosion resistance of TM04 is higher than that of TM40 since Mo is less active than Ti. However, corrosion resistance after mixing Ti and Mo is not as good as single Ti or Mo addition. Elements inside the metal increase, so the galvanic cell reaction intensifies.

Ti and Mo's ability to gain and lose electrons increases, and corrosion resistance decreases with increased x from the previous simulation. The corrosion resistance of the coating decreases with increased x in coatings doped with Mo and Ti. Single Ti and Mo's ability to gain and lose electrons increases with Mo addition from the population analysis mentioned. It is easier to reach the freely corroding potential under electrochemical corrosion; therefore, that of TM13 is lower. TM31 contains more Ti, so a significant passivation zone forms during electrochemical corrosion, with a small free corrosion current. The corrosion resistance of TM31 in coatings doped with Ti and Mo is better than that of the other two coatings.

3.9. Visualization analysis

Fig. 18 illustrates the radar map on the properties of different high-entropy-alloy coatings. TM22 exhibits excellent hardness, wear resistance, high local elastic modulus, and elastic stiffness. TM04 has good corrosion resistance. TM13 showcases excellent resilience but poor corrosion resistance and wear resistance. TM31 and TM40 have no obvious advantages. Besides, TM40 exhibits low hardness. Theoretical guidance is proposed for the formulation of coatings in diverse applications by synthesizing the merits of each coating. TM22 is suitable for occasions demanding high wear resistance and hardness, such as the coating of tool surfaces. TM04 is suitable for occasions demanding high corrosion resistance, such as surface coatings and repair of marine parts.

4. Conclusion

CoCrFeNiTi_(1-x)Mo_x ($x = 0, 0.25, 0.5, 0.75$, and 1) was prepared on the surface of the 45 steel substrate by a powder-presetting method. The work explored the influences of Ti and Mo alloying on the microstructure and properties of laser cladding CoCrFeNi high-entropy alloy. Specific conclusions are as follows.

- (1) The phase formation was predicted by theoretically calculating the standard parameters of the CoCrFeNiTi_(1-x)Mo_x high-entropy alloy. High-entropy-alloy supercells were established, and supercell properties were calculated using CASTEP. CoCrFeNiTi_(1-x)Mo_x, exhibiting mechanical stability, was a ductile material. High-entropy-alloy coating TM22 was predicted to have higher hardness by combining cohesive energy, theoretical hardness calculation, and anisotropic analysis. CoCrFeNiTi_(1-x)Mo_x exhibited metallic character through the maps of the state density and the partial state density.

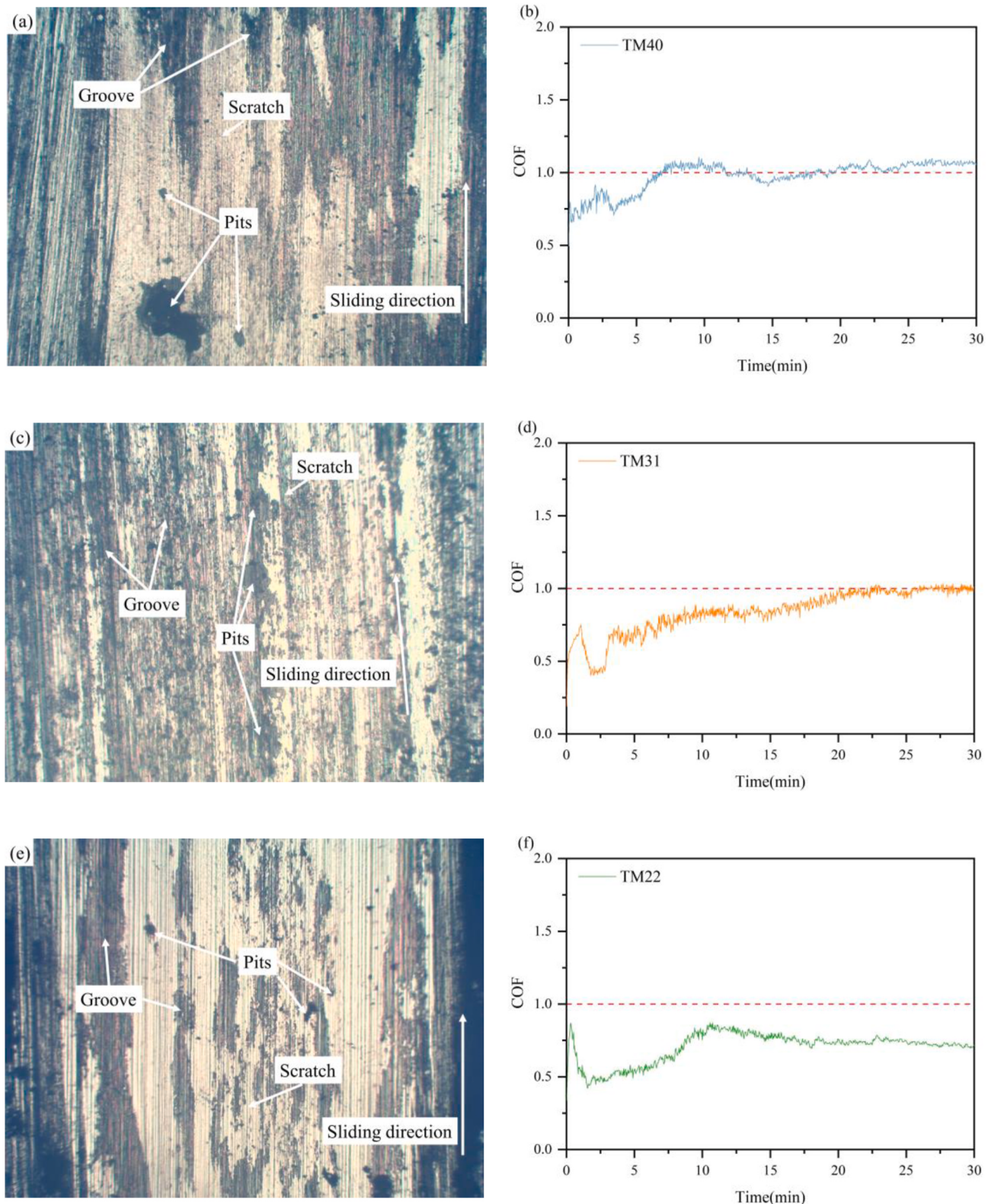


Fig. 11. Wear profile and wear curve diagram: (a–b) Wear profile and wear curve of TM40, (c–d) Wear profile and wear curve of TM31, (e–f) Wear profile and wear curve of TM22, (g–h) Wear profile and wear curve of TM13, (i–j) Wear profile and wear curve of TM04.

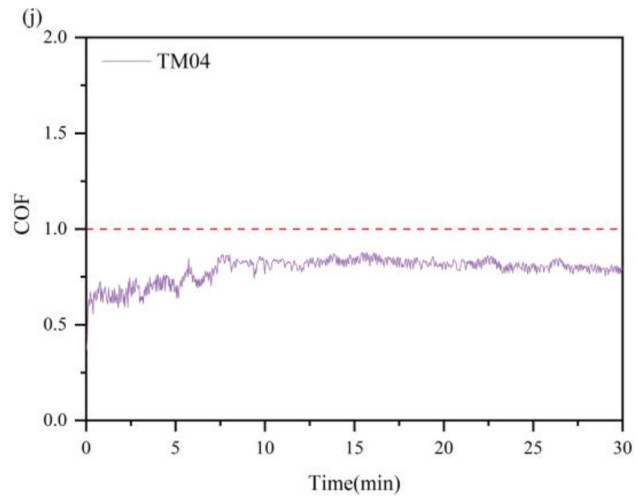
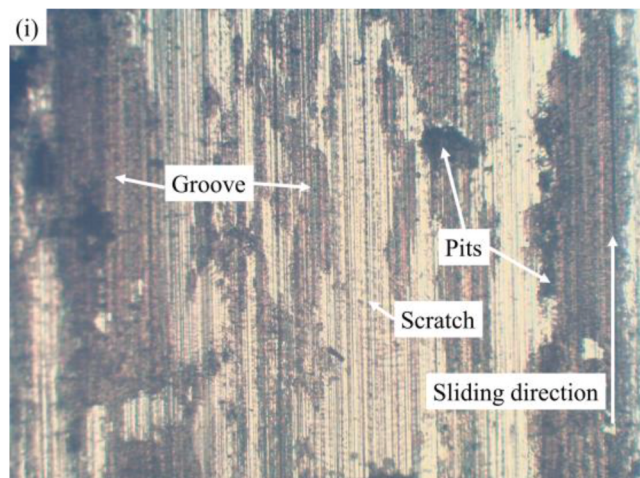
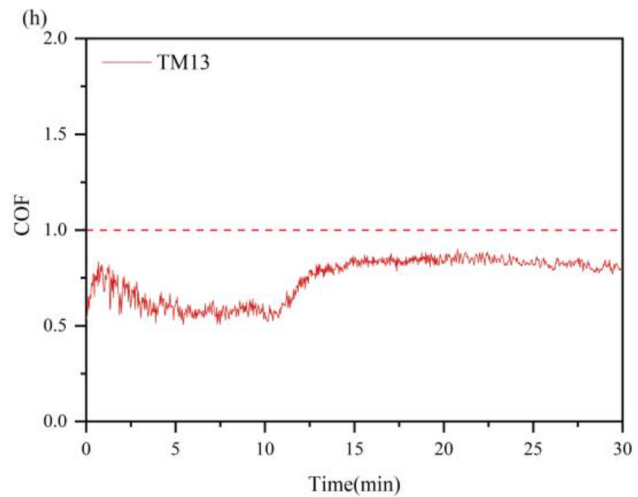
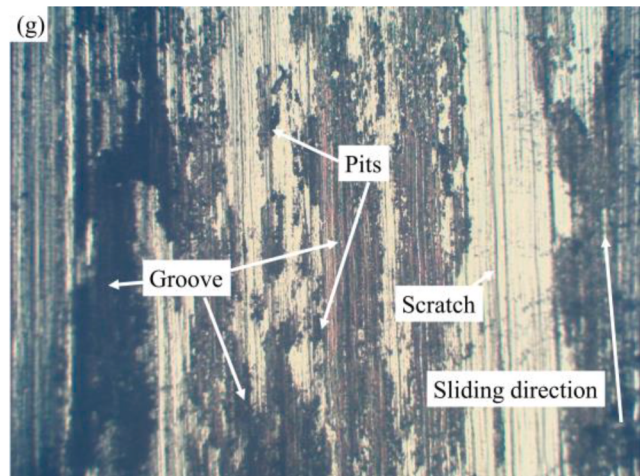


Fig. 11. (continued).

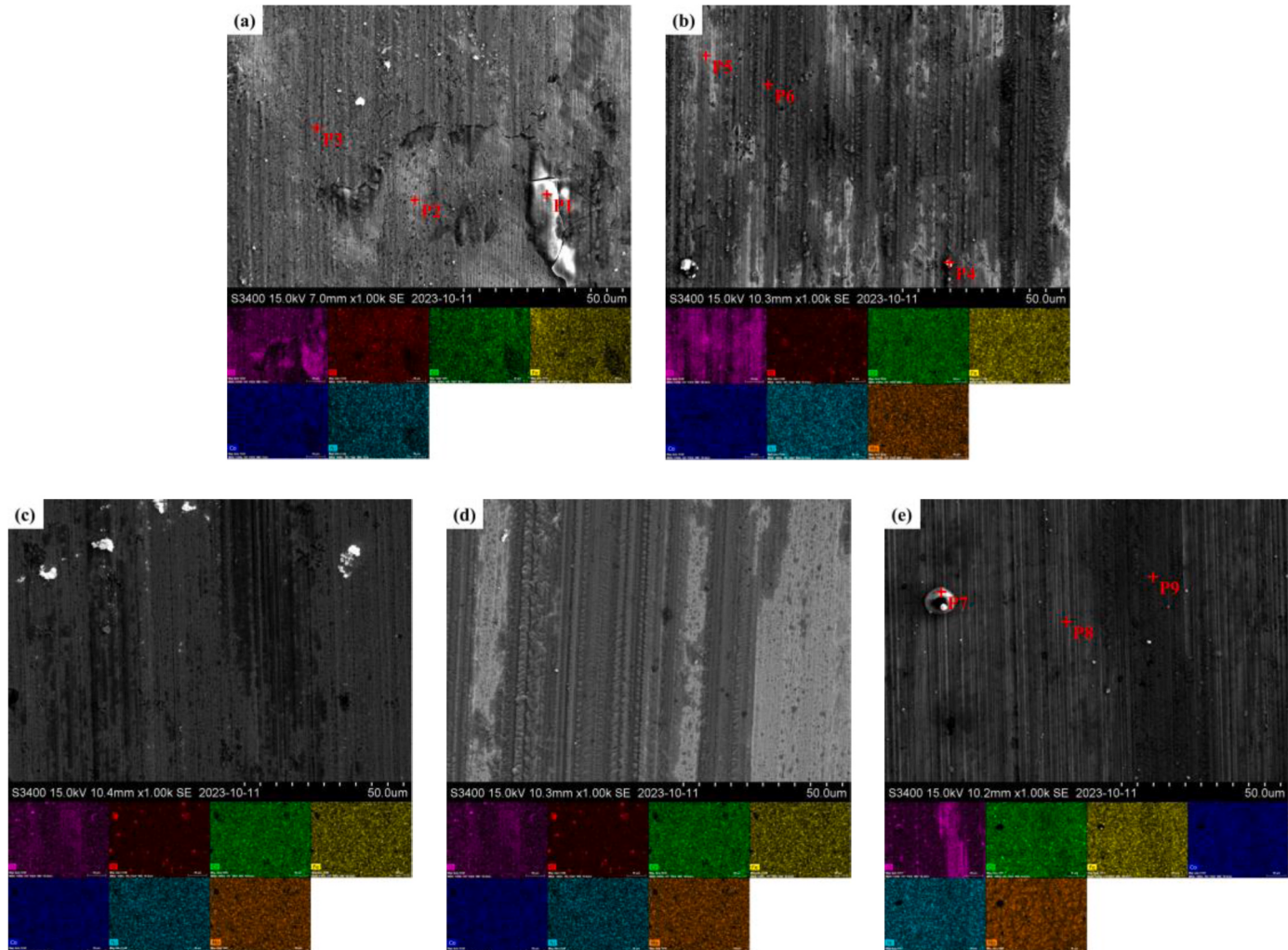


Fig. 12. Elements mapping results of wear surface: (a) TM40, (b) TM31, (c) TM22, (d) TM13, (e) TM04.

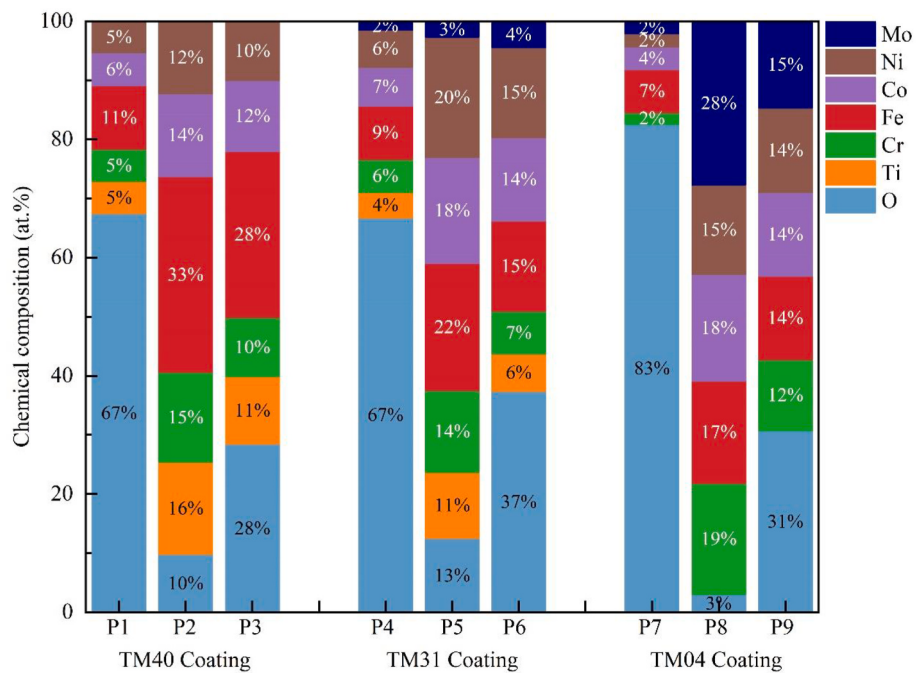


Fig. 13. EDS analysis on the wear surface of the TM40, TM31 and TM04 coating (at.%).

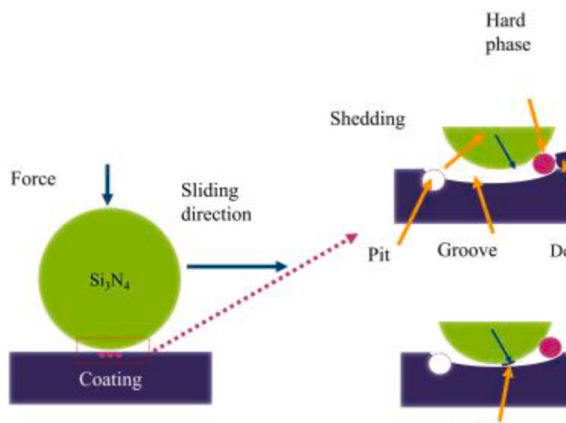


Fig. 14. Diagram of wear form.

Table 10

The electrochemical parameters obtained from the polarization curves of the different HEA coating.

Corrosion area	E_{corr}/V	I_{corr}/A
TM40	-0.770 ± 0.0289	$8.314e-007 \pm 0.348e-007$
TM31	-0.907 ± 0.0320	$5.387e-007 \pm 0.249e-007$
TM22	-0.916 ± 0.0429	$1.581e-006 \pm 0.047e-006$
TM13	-0.997 ± 0.0432	$4.123e-006 \pm 0.069e-006$
TM04	-0.700 ± 0.0327	$7.183e-007 \pm 0.479e-007$

- (2) Five coatings contained the FCC phase, BCC phase, and IMCs, which was consistent with the predicted results of the phase composition from XRD. TM40, TM31, TM22, and TM13 were composed of FCC, BCC, and CoTi₂ phases. TM04 was composed of FCC, BCC, and Co₂Mo₃ phases through XRD and microstructure analysis.
- (3) TM22 had the optimal hardness, high local elastic modulus, and elastic stiffness from microhardness and nano-indentation

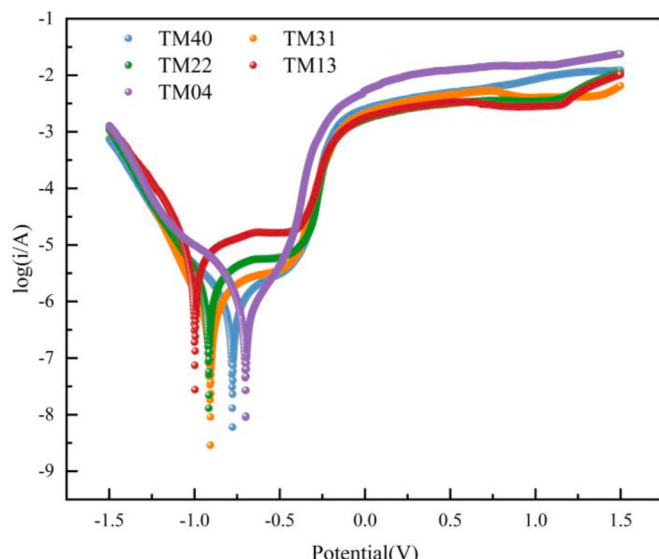


Fig. 15. The potentiodynamic polarization plots of the different HEA coating.

results. Its average microhardness, local elastic modulus, and elastic stiffness were 873.28 HV_{0.5}, 265.5606 GPa, and 102.8008 GPa, respectively. TM04 exhibited a large resilience (35.8156 nm). TM13 had high plasticity to store energy (14634.42×10^{-15} J).

- (4) The wear resistance test and corrosion resistance results showed TM22 exhibited optimal wear resistance, and its COF and wear mass loss were 0.7026 and 0.0410 mm³, respectively. The wear forms of the five coatings were abrasive wear and adhesive wear. TM04 had optimal corrosion resistance, and its self-corrosion voltage and self-corrosion current were -0.700 V and 5.387×10^{-7} A, respectively. The coating with Ti exhibited a significant passivation area, which reduced the corrosion rate during corrosion.

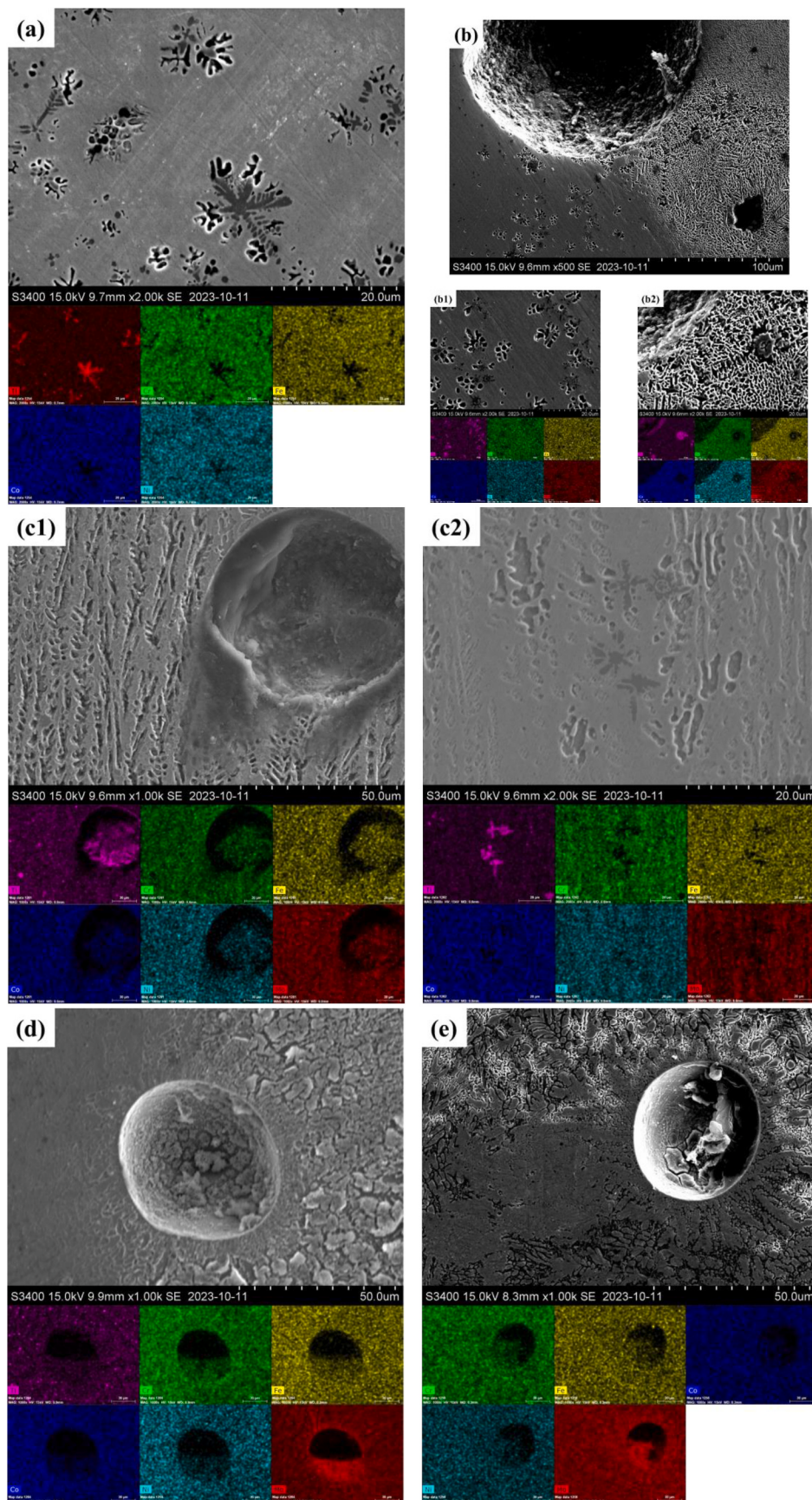


Fig. 16. Elements mapping results of Corroded Surfaces: (a) TM40, (b-b2) TM31, (c1-c2) TM22, (d) TM13, (e) TM04.

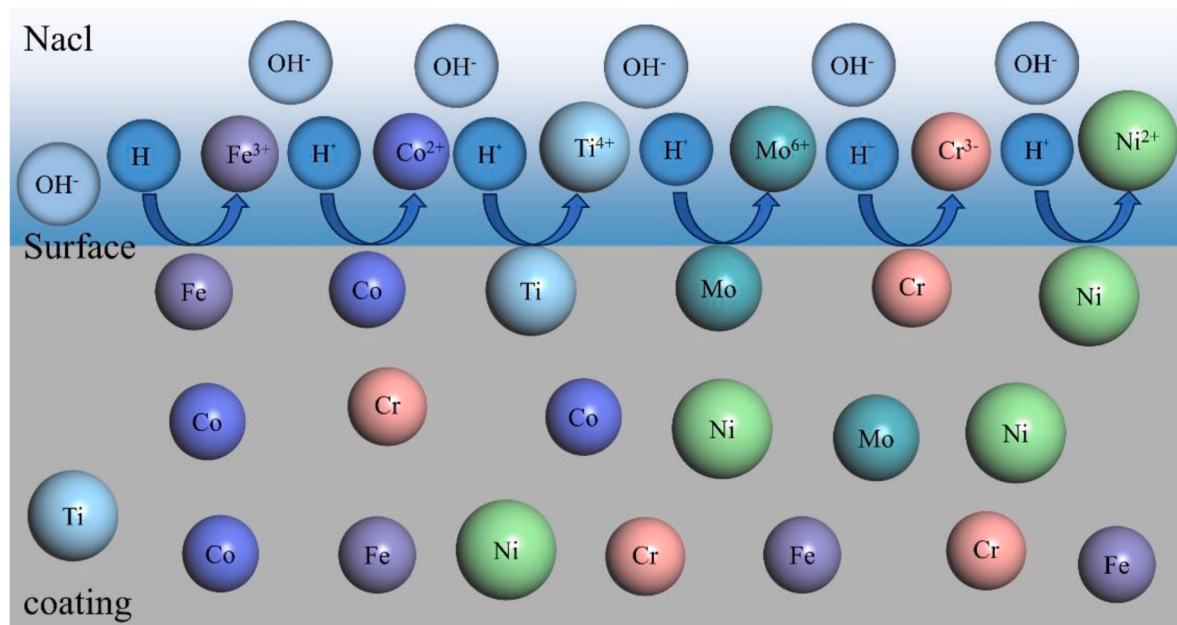


Fig. 17. The mechanism of electrochemical corrosion.

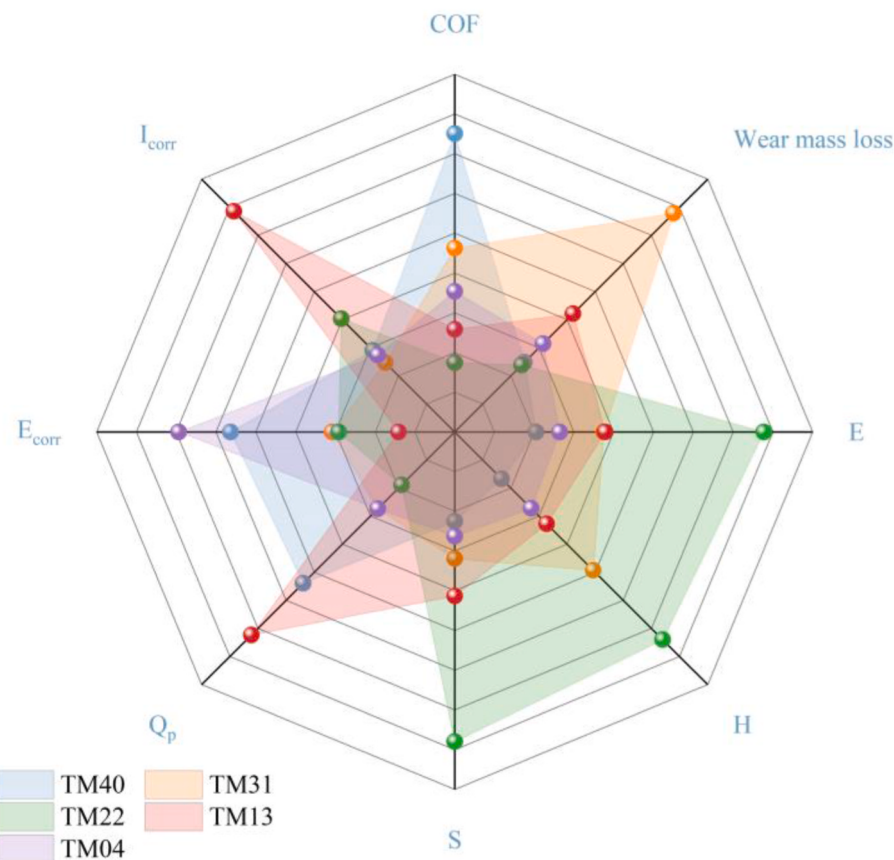


Fig. 18. Radar map of different x added coatings.

There is a certain deviation between the theoretical calculations and the experimental results during the research process. The theoretical calculation of the work focuses on the theoretical calculation of solid-solution high-entropy alloys. It is used to clarify the crystal properties of high-entropy alloys and guide the preparation of high-entropy alloy coatings. The coating prepared during the test contains intermetallic

compounds, so there is a certain deviation between the theoretical calculation and the actual conclusion. The research results can guide the application scenarios for preparing coatings with different advantages and provide a theoretical basis for the laser cladding of high entropy alloys.

Funding

The work was supported by Science and Technology Major Project of Fujian Province (Grant No. 2020HZ03018).

Availability of data and material

The data supporting the conclusions are included in the article.

Authors' contributions

Guofu Lian: Formal analysis, writing – original draft, writing – review and editing, supervision, funding acquisition. Jianghuai Yang: Methodology, investigation, formal analysis, writing – original draft. Changrong Chen: Investigation, formal analysis. Xu Huang: Methodology, investigation. Meiyang Feng: writing – review and editing.

Declaration of interests

The authors declare the following financial interests/personal relationships which may be considered as potential competing interests:

Guofu Lian reports financial support was provided by Science and Technology Major Project of Fujian Province (Grant No. 2020HZ03018).

References

- [1] Zhao Y, Zhang T, Chen L, et al. Microstructure and mechanical properties of Ti–C–TiN-reinforced Ni204-based laser-cladding composite coating. *Ceram Int* 2021;47(5):5918–28.
- [2] Zhu L, Xue P, Lan Q, Meng G, Ren Y, Yang Z, et al. Recent research and development status of laser cladding: a review. *Opt Laser Technol* 2021;138: 106915.
- [3] Liu Y, Ding Y, Yang L, Sun R, Zhang T, Yang X. Research and progress of laser cladding on engineering alloys: a review. *J Manuf Process* 2021;66:341–63.
- [4] Zhang M, Zhou X, Yu X, et al. Synthesis and characterization of refractory TiZrNbWMo high-entropy alloy coating by laser cladding. *Surf Coating Technol* 2017;31:321–9.
- [5] Zhang H, Pan Y, He Y, Jiao H. Microstructure and properties of 6FeNiCoSiCrAlTi high-entropy alloy coating prepared by laser cladding. *Appl Surf Sci* 2011;257(6): 2259–63.
- [6] He F, Wang Z, Wu Q, Niu S, Li J, Wang J, et al. Solid solution island of the Co–Cr–Fe–Ni high entropy alloy. *system* 2017;131:42–6.
- [7] Tian LH, Xiong W, Liu C, Lu S, Fu M. Microstructure and wear behavior of atmospheric plasma-sprayed AlCoCrFeNiTi high-entropy alloy coating. *J Mater Eng Perform* 2016;25:5513–21.
- [8] Liu WH, Lu ZP, He JY, Luan JH, Wang ZJ, Liu B, et al. Ductile CoCrFeNiMox high entropy alloys strengthened by hard intermetallic phases 2016;116:332–42.
- [9] Wang X, Liu Q, Huang Y, Xie L, Xu Q, Zhao T. Effect of Ti content on the microstructure and corrosion resistance of CoCrFeNiTix high entropy alloys prepared by laser cladding. *Materials* 2020;13(10):2209.
- [10] Fu Y, Huang C, Du C, Li J, Dai C, Luo H, et al. Evolution in microstructure, wear, corrosion, and tribocorrosion behavior of Mo-containing high-entropy alloy coatings fabricated by laser cladding. *Corrosion Sci* 2021;191:109727.
- [11] Singh AK, Kumar N, Dwivedi A, et al. A geometrical parameter for the formation of disordered solid solutions in multi-component alloys. *Intermetallics* 2014;53: 112–9.
- [12] Yao XJ, Shi XF, Wang YP, Gan GY, Tang BY. The mechanical properties of high entropy (-like) alloy Wx (TaTiVCr) 1-x via first-principles calculations. *Fusion Eng Des* 2018;137:35–42.
- [13] Osintsev K, Konovalov S, Gromov V, et al. Phase composition prediction of Al–Co–Cr–Fe–Ni high entropy alloy system based on thermodynamic and electronic properties calculations. *Mater Today Proc* 2021;46:961–5.
- [14] Wang Z, Huang Y, Yang Y, et al. Atomic-size effect and solid solubility of multicomponent alloys. *Scripta Mater* 2015;94:28–31.
- [15] Ma Z, Xia C, Zhong H, Yang T, Liu N, Liang C, et al. Microstructure, mechanical property and corrosion resistance of FeCoCrNi-M high-entropy alloy coatings on 6061 aluminum alloy prepared by laser cladding. *Surf Coating Technol* 2023; 129217.
- [16] Dong Y, Lu Y, Jiang L, et al. Effects of electro-negativity on the stability of topologically close-packed phase in high entropy alloys. *Intermetallics* 2014;52: 105–9.
- [17] Li Y, Liu H, Liu X, Chen P, Yang H, Hao J, et al. Microstructure, thermostability and tribological behavior of composite CoCrFeNiTix high-entropy alloy coatings fabricated by laser cladding. *Optik* 2023;283:170899.
- [18] Zhang S, Han B, Li M, Zhang Q, Hu C, Niu S, et al. Investigation on solid particles erosion resistance of laser cladded CoCrFeNiTi high entropy alloy coating. *Intermetallics* 2021;131:107111.
- [19] Gao MC, Niu C, Jiang C, et al. Applications of special quasi-random structures to high-entropy alloys. *High-Entropy Alloys: Fundamentals and Applications* 2016: 333–68.
- [20] Gao MC, Gao P, Hawk JA, Ouyang L, Alman DE, Widom M. Computational modeling of high-entropy alloys: structures, thermodynamics and elasticity. *J Mater Res* 2017;32(19):3627–41.
- [21] Jing P, Wang H, Chen W, Chen L, Yin H, Wu H, et al. Effect of Ti addition on microstructure and tribological properties of laser cladding Ni35/WC coating in an oxygen-free environment. *Surf Coating Technol* 2022;440:128480.
- [22] Guo W, Dmowski W, Noh JY, Rack P, Liaw PK, Egami T. Local atomic structure of a high-entropy alloy: an X-ray and neutron scattering study. *Metall Mater Trans* 2013;44:1994–7.
- [23] Liu H, Gao W, Liu J, et al. Microstructure and properties of CoCrFeNiTi high-entropy alloy coating fabricated by laser cladding. *J Mater Eng Perform* 2020;29: 7170–8.
- [24] Nutor RK, Cao Q, Wang X, Zhang D, Fang Y, Zhang Y, et al. Phase selection, lattice distortions, and mechanical properties in high-entropy alloys. *Adv Eng Mater* 2020; 22(11):2000466.
- [25] Gu Z, Peng W, Guo W, Zhang Y, Hou J, He Q, et al. Design and characterization on microstructure evolution and properties of laser-cladding Ni1. 5CrFeTi2B0. 5Mox high-entropy alloy coatings. *Surf Coating Technol* 2021;408:126793.